Heliyon 11 (2025) e42685

Contents lists available at ScienceDirect

Heliyon

journal homepage: www.cell.com/heliyon

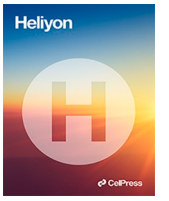

Research article

Cisplatin-loaded UiO-66-NH_2 functionalized with folic acid enhances apoptotic activity and antiproliferative effects in MDA-MB-231 breast and A2780 ovarian cancer cells: An *in vitro* study

Zahra Sadeghi Jam [a], Farzaneh Tafvizi [a,*], Parvin Khodarahmi [a], Parvaneh Jafari [b], Fahimeh Baghbani-Arani [c]

[a] *Department of Biology, Parand Branch, Islamic Azad University, Parand, Iran*
[b] *Microbiology Department, Faculty of Science, Arak Branch, Islamic Azad University, Arak, Iran*
[c] *Department of Genetics and Biotechnology, School of Biological Science, Varamin-Pishva Branch, Islamic Azad University, Varamin, Iran*

ARTICLE INFO

Keywords:
Breast cancer
Ovarian cancer
Metal-organic framework
Cisplatin
Apoptosis
UiO-66-NH_2-CIS-FA

ABSTRACT

The multifunctional nature of UiO-66-NH_2 as a drug carrier positions it as an optimal candidate for encapsulating and delivering anticancer agents. This study developed a folic acid (FA)-functionalized metal-organic framework (MOF) based on UiO-66-NH_2 to facilitate the targeted delivery of cisplatin (CIS) to MDA-MB-231 breast cancer and A2780 ovarian cancer cells. Fourier transform infrared spectroscopy (FT-IR) confirmed the successful encapsulation of CIS within UiO-66-NH_2, while the drug release profile demonstrated a sustained, pH-responsive release of CIS, with a pronounced increase in the acidic tumor microenvironment. The MTT assay revealed excellent biocompatibility of UiO-66-NH_2-FA with HFF healthy cells, whereas UiO-66-NH_2-CIS-FA significantly enhanced anticancer activity against MDA-MB-231 and A2780 cells. Treatment with UiO-66-NH_2-CIS-FA induced substantial apoptosis in both cell lines, leading to a marked upregulation of *BAX* and *P53* gene expression, alongside the downregulation of *BCL2, CCND1,* and *CDK4*. Furthermore, cells treated with CIS, UiO-66-NH_2-CIS, and UiO-66-NH_2-CIS-FA exhibited a significant increase in DCF fluorescence compared to the control group, indicating elevated ROS generation. UiO-66-NH_2-CIS-FA demonstrated enhanced drug-loading capacity and cytotoxic efficacy against cancer cells. Functionalization of UiO-66-NH_2-CIS with FA presents a promising strategy for targeted cancer therapy by improving drug delivery specificity and enhancing therapeutic outcomes.

1. Introduction

Breast and ovarian cancers exhibit a complex etiology involving both genetic and non-genetic factors, contributing to their high heterogeneity. According to recent global cancer statistics, breast cancer accounted for 11.7 % of newly diagnosed cancer cases in

* Corresponding author.
E-mail addresses: zahrasadeghijam@gmail.com (Z. Sadeghi Jam), farzanehtafvizi54@gmail.com, Farzaneh.Tafvizi@iau.ac.ir (F. Tafvizi), khodarahmiparvin@yahoo.com (P. Khodarahmi), parvaneh.jafari@gmail.com, p-jafari@iau-arak.ac.ir (P. Jafari), baghbani.f@gmail.com (F. Baghbani-Arani).

https://doi.org/10.1016/j.heliyon.2025.e42685
Received 19 September 2024; Received in revised form 1 February 2025; Accepted 12 February 2025
Available online 14 February 2025

2020, surpassing lung cancer as the most frequently diagnosed malignancy worldwide [1]. Ovarian cancer ranks fifth in cancer-related mortality among women in industrialized countries and represents the sixth most prevalent cancer globally [2]. These malignancies necessitate urgent therapeutic and diagnostic interventions [3,4]. Platinum-based compounds are widely employed in the treatment of various cancers, including ovarian, bladder, breast, lung, head, and neck malignancies [5]. Cisplatin (CIS), a commonly utilized platinum-based chemotherapeutic agent, is particularly effective in treating several subtypes of breast cancer [6]. CIS exerts its anticancer activity by inducing DNA damage through the formation of platinum-DNA adducts, leading to G1/S cell cycle arrest and apoptosis. Studies have demonstrated that CIS targets multiple pathways to exert its therapeutic effects, often binding to mitochondrial DNA (*mtDNA*) or genomic DNA (*gDNA*) to form DNA lesions, inhibit the synthesis of proteins, messenger RNA (*mRNA*), and DNA, disrupt DNA replication, and activate transduction pathways that ultimately result in necrosis or apoptosis [7]. However, the clinical use of CIS is associated with significant adverse effects, including nephrotoxicity and neurotoxicity. Tumor-targeted drug delivery platforms offer a promising approach to delivering therapeutic agents directly to tumor sites, enhancing treatment efficacy while reducing off-target toxicity in normal tissues [8].

Nanomedicine and nano-delivery platforms represent emerging interdisciplinary fields that focus on utilizing nanoscale materials for diagnostic applications and targeted therapeutic delivery. Nanotechnology presents promising opportunities for the treatment of chronic human diseases, including cancer, by enabling precise drug delivery to specific sites [9,10].

Metal-organic frameworks (MOFs) are hybrid porous materials synthesized through the coordination of metal ions with organic ligands [11]. The first identification of these advanced porous materials occurred in the late 1980s when Robson and Hoskins engineered specific spatial topologies by coordinating multi-dentate ligands with metal centers. The application of MOFs as solid catalysts or catalyst supports in various chemical transformations has demonstrated significant potential [12,13]. As biomaterials, MOFs exhibit advantageous properties such as high pore volume, large internal surface area, uniform porosity, and remarkable stability [14,15]. The exceptional characteristics of MOFs have facilitated their extensive utilization in various biomedical applications, including enzyme catalysis, gas storage, pH sensing, diagnostics, photovoltaic applications, and drug delivery [16]. The physical and chemical properties of MOFs, along with their unique structural versatility, allow for extensive customization [17]. Several MOFs containing metals such as chromium (Cr), iron (Fe), zinc (Zn), and zirconium (Zr) have been employed as drug delivery systems [16]. Given the potential toxicity associated with chromium-based compounds, alternative low-toxicity metals have been explored in MOF synthesis. Zirconium-based MOFs have gained widespread attention due to their non-toxic nature, superior stability, and biocompatibility with living systems [18].

Zirconium's exceptional biocompatibility has driven extensive research on its MOFs, including the well-characterized Zr terephthalate UiO-66 for drug delivery applications. UiO-66 consists of $[Zr_6O_4(OH)_4]$ octahedral clusters coordinated with benzene-1,4-dicarboxylic acid (BDC) ligands [19].

In recent years, MOFs have garnered substantial interest for their potential in drug delivery systems, particularly in cancer therapy. Among these, UiO-66-NH_2 has emerged as a promising candidate due to its high surface area, tunable porosity, and excellent biocompatibility. Various functionalized UiO-66 derivatives have been explored for encapsulating anticancer drugs, benefiting from their remarkable chemical and physical properties, including exceptional water resistance, superior chemical, thermal, and mechanical stability, optimal biodegradability, and extensive surface area [20]. He et al. reported a Zr-based MOF designed for the delivery of CIS, which enhanced its therapeutic efficacy by overcoming drug resistance in ovarian cancer cells [21]. Anticancer agents such as 5-fluorouracil (5-FU) and doxorubicin have been successfully encapsulated within UiO-66 MOFs, demonstrating significant potential in inhibiting the proliferation of breast and ovarian cancer cells in experimental models [22–24]. Orellana-Tavra et al. investigated the transport of the hydrophilic drug calcein within the UiO-66 framework, highlighting its suitability for controlled drug release applications [25]. Nasrabadi et al. synthesized UiO-66 via a solvothermal technique to achieve the controlled release of ciprofloxacin, further expanding the biomedical applications of these frameworks [26].

UiO-66-NH_2 has been utilized for the pH-dependent delivery of quercetin, exhibiting sustained release and significant cytotoxic effects against MDA-MB-231 breast cancer cells through apoptosis induction. Studies have highlighted the potential of Fe_3O_4-COOH@UiO-66-NH_2 as a targeted nanocarrier for anticancer drug delivery [27]. This framework has also been employed for the delivery of curcumin, effectively addressing its low bioavailability and solubility challenges. The release of curcumin from UiO-66-NH_2 was found to be pH-dependent, with a favorable biocompatibility profile, indicating its potential for safe drug administration [28]. In colorectal cancer models, UiO-66-NH_2 loaded with oxaliplatin exhibited enhanced anticancer efficacy by significantly inhibiting cell proliferation and migration compared to the free drug [29].

Doxorubicin-loaded UiO-66-NH_2 demonstrated controlled release and high biocompatibility, leading to a significant reduction in adverse side effects compared to free doxorubicin [30]. UiO-66-NH_2/DOX exhibited maximum cytotoxicity against A549 lung cancer cells at a concentration of 100 μg/mL [31].

The tumor microenvironment is increasingly recognized as a key factor influencing cancer treatment outcomes [32]. The integration of molecular targeting agents, such as antibodies, peptides, and folic acid (FA), into nanoscale drug delivery systems has shown significant promise [33,34]. FA, a single-chain glycoprotein, is overexpressed in several cancer types, including ovarian, breast, head and neck, brain, and lung cancers, due to its high affinity for the folate receptor, which is expressed at low levels in normal cells. The overexpression of folate receptors on cancer cell surfaces facilitates enhanced cellular uptake of FA-functionalized drug carriers [35].

Functionalization of UiO-66-NH_2 MOFs with chitosan-folic acid (CS-FA) for the targeted delivery of doxorubicin (DOX) has demonstrated a sustained release profile, particularly under acidic conditions mimicking the tumor microenvironment. At pH 5.2, 39.76 % of DOX was released, compared to only 5.84 % at physiological pH. *In vitro* studies have shown significant cytotoxic effects against MCF-7 breast cancer cells, highlighting the potential of polymer-conjugated nanoparticles in enhancing tumor-targeting efficiency [36].

Similarly, FA-MOF/Bufalin exhibited superior tumor suppression compared to free Bufalin, demonstrating that surface modification of nanoparticles with targeting ligands can enhance drug accumulation at tumor sites and improve therapeutic efficacy [37].

The significance of this research lies in addressing the limitations of conventional drug delivery methods, which often suffer from challenges such as poor bioavailability and non-specific distribution. The utilization of MOF-based nanocarriers offers a promising solution by enabling precise drug delivery to cancer cells, thereby increasing drug concentrations at tumor sites while minimizing systemic toxicity.

This study is the first to report the synthesis of CIS-encapsulated UiO-66-NH_2 decorated with FA, demonstrating substantial improvements in apoptosis induction and cell cycle arrest in MDA-MB-231 and A2780 cancer cell lines. These findings underscore the potential of this nanocarrier as a targeted therapeutic platform, offering novel insights into cancer nanomedicine and precision drug delivery strategies.

2. Materials and methods

2.1. Synthesis of UiO-66-NH_2-CIS-FA

A solution was prepared by dissolving 0.39 g of 2-amino terephthalic acid (Sigma-Aldrich, Germany) and 0.54 g of $ZrCl_4$ in 31 mL of DMF at 25 °C to synthesize UiO-66-NH_2.The mixture was continuously stirred until a clear solution was obtained. The resulting solution was then transferred to a Teflon-lined hydrothermal autoclave and heated at 120 °C for 24 h. After cooling to room temperature, the obtained particles underwent three cycles of centrifugation followed by 15 min of ultrasonic treatment in DMF and chloroform to replace residual DMF and remove unreacted materials. A five-day solvent exchange procedure was performed by immersing the sample in 15 mL of fresh chloroform daily, with 15 min of sonication each day. The final product was pressure-dried at 120 °C to eliminate residual solvents.

For CIS incorporation, CIS (Sobhan Darou Co., Iran) was first dissolved in dimethyl sulfoxide (DMSO) and dispersed in phosphate-buffered saline (PBS) (Gibco, USA) at a concentration of 0.25 mg/mL. This solution was mixed with 10 mg of synthesized MOFs and stirred for 24 h. The resulting slurry was washed three times with ethanol and distilled water, followed by centrifugation at 12,000 rpm for 20 min [38]. The UiO-66-NH_2-CIS particles were subsequently dispersed in an aqueous FA solution (20 mg/mL) in a glass tube with a phenolic cap and ultrasonicated (50 kHz, 100 W/L) for 5 min. The tube was then wrapped in foil to prevent light exposure and agitated for 24 h. The UiO-66-NH_2-CIS-FA particles were isolated by centrifugation at 4000 rpm for 10 min and washed three times with deionized water. The final product was reconstituted in deionized water and subjected to freeze-drying for 48 h [39].

2.2. Characterization of UiO-66-NH_2-CIS-FA nanoparticles

The functional groups of CIS, UiO-66-NH_2, UiO-66-NH_2-CIS, and UiO-66-NH_2-CIS-FA were characterized using FT-IR with a Spectrum Two spectrometer (PerkinElmer, USA). Spectra were recorded over a wavelength range of 400–4000 cm^{-1}. The morphological characteristics of the MOFs were analyzed using SEM with a TESCAN VEGA 3SB instrument and TEM with a Philips CM30 instrument (Philips, Netherlands). For TEM analysis, a small quantity of UiO-66-NH_2-CIS-FA was deposited onto a carbon-coated copper grid and stained with 1 % phosphotungstic acid.

The hydrodynamic diameter and size distribution of UiO-66-NH_2-CIS-FA were determined using DLS with a Malvern Zetasizer Nano instrument (Malvern Instruments, Worcestershire, UK). The crystallographic structure of UiO-66-NH_2-CIS-FA was evaluated by XRD using a Bruker AXS D8 Advance diffractometer with Cu Kα radiation, scanning within the 2θ range of 10°–90°.

2.3. Entrapment efficiency (EE %)

The entrapment efficiency (EE) of CIS was determined by quantifying the concentration of unencapsulated drugs. Free CIS was separated from the UiO-66-NH_2-CIS-FA dispersion using Ultracel-30K Millipore filters with a molecular weight cutoff (MWCO) of 30,000 Da. A volume of 500 μL of the formulation was placed in the inner compartment of the filtration device and centrifuged at 4000×*g* for 20 min at 4 °C using a cooling centrifuge (Eppendorf® 580R, Germany). The concentration of unencapsulated CIS in the filtrate was analyzed by UV–visible spectrophotometry at 510 nm using a JASCO V-530 spectrophotometer (JASCO, Japan). The EE was calculated using the following equation (EQ1) [20].

$$\text{Equation 1 : EE } (\%) = \frac{\text{Initial cisplatin added} - \text{Free cisplatin}}{\text{Initial cisplatin added}} \times 100$$

2.4. In vitro release study and kinetic model

The release of CIS from UiO-66-NH_2-CIS and UiO-66-NH_2-CIS-FA was evaluated using the dialysis diffusion bag method with a molecular weight cutoff (MWCO) of 12 kDa (Merck, Germany). A total of 2 mL of the MOF suspension was placed into a dialysis bag and sealed. The sealed bag was then immersed in 50 mL of phosphate-buffered saline containing sodium dodecyl sulfate (PBS-SDS) at pH 5.4 and 7.4, maintained at 37 °C, which served as the release medium and receiver medium, respectively. The system was placed on a magnetic stirrer set at 300 rpm. Samples were withdrawn from the buffer compartment at predetermined intervals and replaced with fresh PBS-SDS (Merck, Germany) to maintain sink conditions. The optical density (OD) of the collected samples was measured at 510

nm using a UV–visible spectrophotometer, and the concentration of released CIS was determined using a standard calibration curve. A cumulative release profile was plotted to illustrate the drug release behavior over time [40].

To analyze the release kinetics of CIS, various mathematical models were employed. These included the zero-order model (EQ2), which describes the cumulative percentage of drug release over time; the first-order model (EQ3), which represents the cumulative percentage of drug remaining over time; the Higuchi model (EQ4), which describes the cumulative percentage of drug release as a function of the square root of time; and the Korsmeyer-Peppas model (EQ5), which establishes a relationship between the logarithm of cumulative drug release and the logarithm of time [40].

Equation (2): Zero-order Model

$$C_t = C_0 + K_0 t$$

This equation describes the relationship between the amount of drug dissolved at time t (C_t), the initial drug concentration (C_0), and the zero-order release constant (K_0).

Equation (3): First-order Model

$$\text{Log } C = \text{Log}C_0 - Kt/2.303 \text{ or } C_t = C_0\, e^{-kt}$$

This equation characterizes first-order drug release kinetics, where C_t represents the amount of drug released at time t, C_0 is the initial drug concentration, K is the first-order release constant, and t represents time.

Equation (4): higuchi model

$$Q = K_H t^{1/2}$$

The Higuchi model describes the relationship between drug release and time, where Q represents the cumulative amount of drug released at time t, and KH is the Higuchi dissolution constant.

Equation (5): Korsmeyer-Peppas Model

$$M_t / M_\infty = K_{kp} t^n$$

This model establishes a relationship between the fraction of drugs released (M_t/M_∞) at a given time t, where M_t is the drug released at time t, M_∞ is the total drug released at equilibrium, K_{kp} is the release rate constant, and n is the release exponent, which characterizes the drug release mechanism.

2.5. Physical stability assay

UiO-66-NH_2-CIS-FA stability was assessed over 30 days at 25 ± 2 °C and 4 ± 2 °C. At specified intervals (14 and 30 days), dynamic particle size, PDI, and EE% were measured and compared with fresh formulations to evaluate changes in physicochemical properties.

2.6. Cytotoxicity assay

Three cell lines, MDA-MB-231, A2780, and human foreskin fibroblast cells (HFF) cells, obtained from the National Center for Genetic and Biological Resources of Iran, were cultured in RPMI 1640 and Dulbecco's Modified Eagle Medium (DMEM) (Gibco, USA). Each cell line was seeded at a density of 1×10^4 cells per well in 96-well tissue culture plates and incubated at 37 °C with 5 % CO_2 for 24 h. Various concentrations (12.5–200 μg/mL) of UiO-66-NH_2, free CIS, UiO-66-NH_2-CIS, and UiO-66-NH_2-CIS-FA were added to the wells in triplicate and incubated at 37 °C with 5 % CO_2 for 48 and 72 h. Following incubation, cells were treated with 100 μL of 3-(4,5-Dimethylthiazol-2-yl)-2,5-Diphenyltetrazoliumbromid (MTT) (Sigma-Aldrich, Germany) and incubated at 37 °C with 5 % CO_2 for 4 h. After incubation, 100 μL of DMSO was added to each well following the removal of the medium. The absorbance of the formed formazan product was measured using a microplate reader (Biotek, USA).

Cell viability for all treatments was calculated using the following equation (EQ6) [41]:

$$\text{Equation 6 : Cell viability } (\%) = \left(\frac{\text{Absorption treatment} - \text{Absorption blank}}{\text{Absorption control} - \text{Absorption blank}}\right) \times 100$$

2.7. Apoptotic and cell cycle-associated genes expression analysis

MDA-MB-231 and A2780 cells were treated with UiO-66-NH_2, free CIS, UiO-66-NH_2-CIS, and UiO-66-NH_2-CIS-FA at IC_{50} concentrations for 48 h. Total RNA was extracted using an RNA extraction kit (Cinnagen, Iran), and complementary DNA (cDNA) was synthesized using the RevertAid™ cDNA synthesis kit (Cinnagen, Iran). The expression levels of B-cell leukemia/lymphoma 2 (*BCL2),* BCL2 Associated X *(BAX),* Tumor protein P53 *(P53),* CyclinD1 *(CCND1),* and Cyclin-dependent kinase 4 *(CDK4)* were analyzed by real-time polymerase chain reaction (PCR). The expression of *β-actin* was used as an internal control.

The real-time PCR program consisted of an initial denaturation at 95 °C for 10 min, followed by 35 cycles of 95 °C for 15 s, 57 °C for 15 s, and 72 °C for 20 s, with a final extension step at 72 °C for 1 min.

Amplification reactions were performed in a total volume of 20 μL using SYBR® Green Master Mix (Bio-Rad, USA), and the PCR products were analyzed by electrophoresis on a 2 % agarose gel. Gene expression data were quantified using the Rotor-Gene Q real-

time detection system (Qiagen, USA), and relative gene expression levels were calculated based on the ΔΔCt method, assuming optimal PCR efficiency [42–44].

2.8. Flow cytometry for apoptosis/necrosis rate

Apoptotic cell detection was performed using the Annexin V-FITC/propidium iodide (PI) apoptosis kit (MabTag GmbH, Germany). MDA-MB-231 and A2780 cells were seeded in a cell culture plate at a density of 5×10^5 cells per well and incubated overnight at 37 °C with 5 % CO_2 to allow for cell attachment. Cells were then treated individually with UiO-66-NH_2, free CIS, UiO-66-NH_2-CIS, and UiO-66-NH_2-CIS-FA at IC_{50} concentrations for 48 h. Following treatment, cells were washed twice with cold, sterile PBS (pH 7.4), and 5×10^5 cells per well were resuspended in 1X binding buffer provided in the kit. According to the manufacturer's instructions, appropriate amounts of PI (red fluorescence) and Annexin V-FITC (green fluorescence) were added to the cell suspension, followed by incubation at room temperature for 10 min in the dark. Finally, the stained cell suspensions were transferred to flow cytometry tubes and analyzed using flow cytometry (FACSCalibur, BD Biosciences, Singapore) [45].

2.9. Cell cycle analysis

Cell proliferation was evaluated using PI staining, which allows for the determination of cell cycle stages based on DNA content, as PI binds stoichiometrically to DNA. Cells were seeded in 6-well plates at a density of 1×10^6 cells per well in a complete medium and incubated overnight. Following incubation and three washes with PBS, cells were treated with UiO-66-NH_2, free CIS, UiO-66-NH_2-CIS, and UiO-66-NH_2-CIS-FA for 48 h. After treatment, cells were harvested and fixed in 70 % cold ethanol at 4 °C overnight. Subsequently, cells were stained with 500 μL of PI solution containing RNase and incubated in the dark for 20 min at room temperature. Flow cytometry analysis was performed to assess DNA content. All experiments were conducted in triplicate to ensure reproducibility [46].

2.10. Assay for intracellular reactive oxygen species (ROS) generation

ROS levels generated in response to each treatment were assessed using the DCFDA (2′,7′-dichlorodihydrofluorescein diacetate) ROS Assay Kit KROS96. A2780 and MDA-MB-231 cancer cell lines were treated with CIS and nanoformulations at their IC_{50} concentrations for 48 h, followed by rinsing with PBS. Subsequently, cells were incubated with 100 μL of DCFDA reagent at 37 °C for 45 min in the dark. The fluorescence emission intensity was then measured using a microplate reader to quantify ROS levels [41].

2.11. Statistical analysis

The values are presented as the mean ± SD based on a minimum of three replicates. Statistical analysis was performed using one-way and two-way analysis of variance (ANOVA). Graphs were generated using GraphPad Prism 9 software (GraphPad Software, USA). A *p*-value of less than 0.05 was considered statistically significant.

3. Results and discussion

3.1. Characterization of UiO-66-NH_2-CIS-FA

3.1.1. Size and Dispersity

DLS analysis revealed that the particle sizes of UiO-66-NH_2, UiO-66-NH_2-CIS, and UiO-66-NH_2-CIS-FA were 169.4 ± 6.10 nm, 194.7 ± 5.85 nm, and 236.2 ± 6.74 nm, respectively. The findings suggest that with an average size of around 200 nm, the formulated nanoparticles are suitable for targeted CIS delivery (Table 1 and Fig. 1A). Table 1 also indicates the homogeneous dispersion of the particles, as evidenced by the PDI values of 0.138 ± 0.008 for UiO-66-NH_2, 0.114 ± 0.021 for UiO-66-NH_2-CIS, and 0.208 ± 0.021 for UiO-66-NH_2-CIS-FA), confirming a uniform size distribution.

SEM and TEM analyses were conducted to investigate the surface morphology and structural characteristics of UiO-66-NH_2-CIS-FA, as shown in Fig. 1B and C. The SEM image (Fig. 1B) demonstrates that the nanoparticles retain a uniform spherical morphology without significant degradation or structural abnormalities. Similarly, the TEM image (Fig. 1C) confirms the presence of well-dispersed, spherical structures.

Table 1 further shows that the EE% values for UiO-66-NH_2-CIS and UiO-66-NH_2-CIS-FA were 70.68 ± 1.21 % and 71.52 ± 1.15 %, respectively. In a study by Ronaghi et al., UiO-66 loaded with letrozole exhibited an optimal size of 160 nm, a PDI of 0.188, and an EE% of 62.21 % [47]. Additionally, another study reported that UiO-66-curcumin nanoparticles had a PDI of approximately 0.158 and an EE

Table 1
The main physicochemical parameters (size, PDI, and EE%), were measured immediately after the preparation of MOFs.

Formulations	Size (nm)	PDI	EE (%)
UiO-66-NH_2	169.4 ± 6.10	0.138 ± 0.008	–
UiO-66-NH_2-CIS	194.7 ± 5.85	0.114 ± 0.021	70.68 ± 1.21
UiO-66-NH_2-CIS-FA	236.2 ± 6.74	0.208 ± 0.021	71.52 ± 1.15

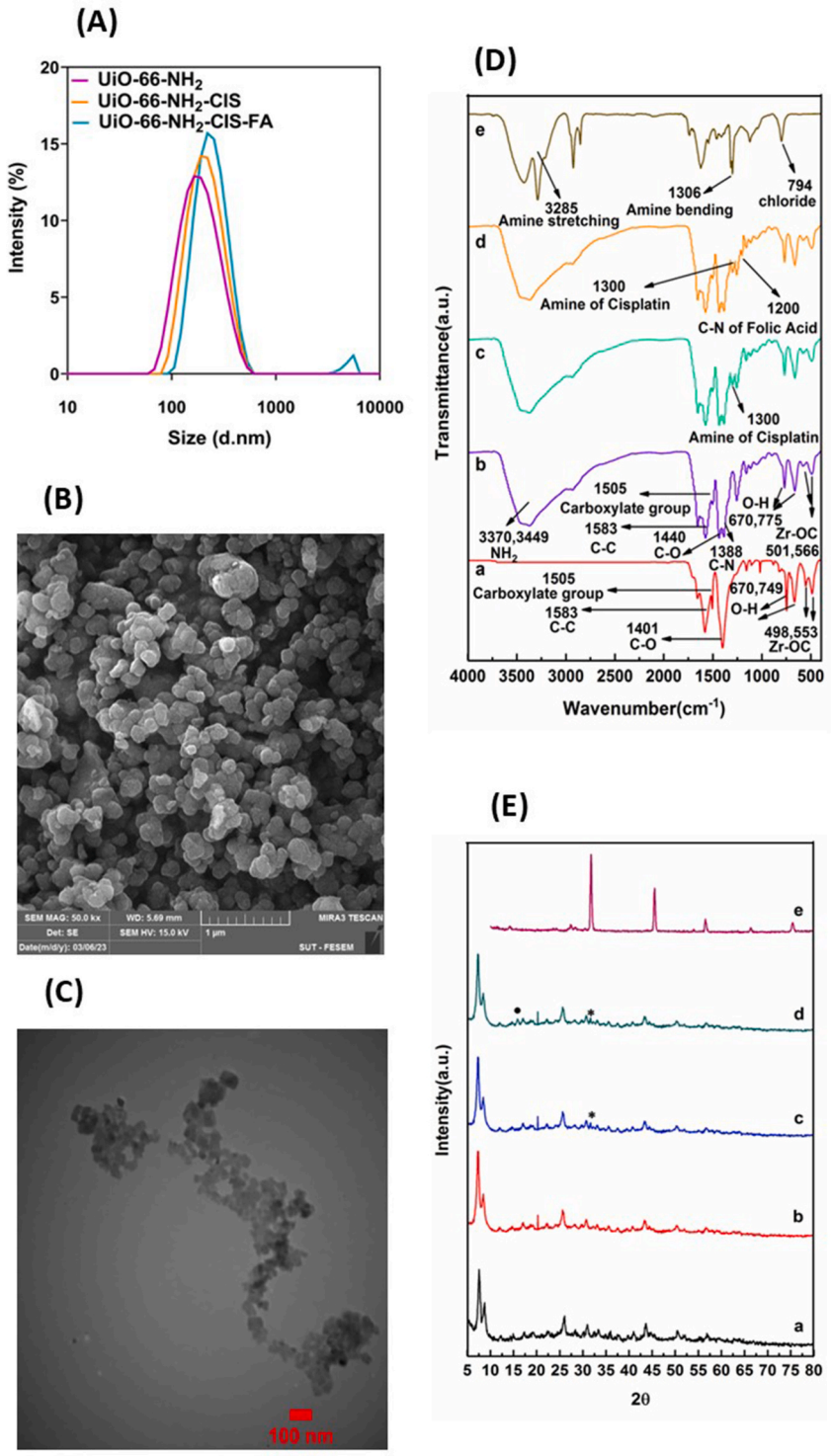

Fig. 1. Following the encapsulation of CIS in the UiO-66-NH_2-FA, the physicochemical characterization of UiO-66-NH_2-CIS-FA was carried out by measuring: (A) DLS techniques, (B) SEM, (C) TEM, (D) FT-IR spectrum and (E) XRD peaks of (a) UiO-66, (b) UiO-66-NH_2, (c) UiO-66-NH_2-CIS, (d) UiO-66-NH_2-CIS-FA and (e) CIS.

% of 65.37 % [20]. The observed differences in PDI and EE% compared to the current study may be attributed to the functionalization of UiO-66-NH_2 with FA groups.

Due to their large pore diameter and high surface area, MOFs can encapsulate substantial amounts of therapeutic agents, making

them highly suitable for drug delivery applications [48]. The substantial drug-loading capacity of MOFs allows for sustained release over an extended period, which is crucial for effective treatment [49]. Nanoparticles within the size range of 100–200 nm are capable of passive accumulation within tumors through the enhanced permeability and retention (EPR) effect, facilitating deeper penetration into solid tumors while minimizing filtration by the liver and spleen [50].

3.1.2. FT-IR and XRD analysis

FT-IR is primarily employed for qualitative assessment, facilitating the identification of functional groups and the elucidation of organic, inorganic, or hybrid structures [51]. FT-IR spectroscopy was used to characterize the structural properties and chemical interactions within the samples [51,52]. The FT-IR spectrum of UiO-66-NH_2 exhibited characteristic peaks at 501 and 566 cm^{-1} (Zr–(OC) symmetric stretching), 1388 cm^{-1} (C-N vibrational stretching of aromatic amines), 1505 cm^{-1} (in- and out-of-phase stretching modes of the carboxylate group), 3370 cm^{-1} (symmetric NH_2), and 3449 cm^{-1} (asymmetric NH_2). In UiO-66-NH_2, NH_2 Absorption peaks corresponding to NH_2 were observed at 3370 and 3449 cm^{-1} (Fig. 1D (a and b)).

The FT-IR spectrum of CIS displayed characteristic peaks at 3285 cm^{-1} (amine stretching), 1306 cm^{-1} (symmetric amine bending), and 794 cm^{-1} (chloride stretching) (Fig. 1D (e)). Upon encapsulation of CIS within UiO-66-NH_2, the symmetric amine bending band of CIS appeared at 1306 cm^{-1}, indicating successful drug loading (Fig. 1D (c)). Additionally, the attachment of FA to UiO-66-NH_2-CIS resulted in the appearance of a C-N stretching band at 1200 cm^{-1}, confirming successful FA conjugation (Fig. 1D (d)). The FT-IR spectra of UiO-66-NH_2 were consistent with previously reported data, demonstrating the structural changes occurring during the synthesis and drug encapsulation processes [52,53].

X-ray diffraction (XRD) is a direct method for determining the crystalline structure and phase composition of materials, as it involves the scattering of X-rays by atoms within a crystal lattice, producing characteristic diffraction patterns [53]. In this study, XRD analysis was conducted to examine the crystalline structure of UiO-66-NH_2-CIS-FA (Fig. 1E).

The XRD pattern of UiO-66 displayed characteristic peaks at 7.56°, 8.68°, 12.15°, 14.90°, 17.30°, 19.17°, 22.63°, 25.95°, 27.58°, 30.17°, 31.08°, 33.46°, 35.87°, 37.71°, 39.72°, 40.91°, 43.77°, 44.77°, 50.57°, 51.94°, and 57.01°, with prominent peaks at 7.56°, 8.68°, and 25.95° considered as index peaks (Fig. 1E (a)). The XRD pattern of UiO-66-NH_2 exhibited peaks at 7.10°, 8.47°, 12.02°, 14.55°, 17.09°, 18.78°, 20.25°, 22.17°, 25.58°, 29.01°, 29.80°, 30.71°, 33.12°, 35.67°, 37.51°, 39.55°, 40.83°, 43.40°, 44.51°, 50.38°, 51.85°, and 56.73°, with characteristic peaks at 8.47°, 7.10°, and 25.58°, and an additional peak at 20.25° associated with NH_2 groups (Fig. 1E (b)).

The XRD pattern of CIS revealed peaks at 27.32°, 31.63°, 45.58°, 55.49°, 66.38°, and 75.51° (Fig. 1E (e)). Upon CIS loading, the diffraction peaks of UiO-66-NH_2 exhibited slight shifts to lower angles, suggesting increased lattice spacing and successful drug incorporation. A distinct peak corresponding to CIS was observed at 31.66°, marked with an asterisk (*) (Fig. 1E (c)).

The presence of FA within the UiO-66-NH_2-CIS structure was confirmed by the appearance of a peak at 16.30°, marked with a circle (●), further validating FA conjugation (Fig. 1E (d)).

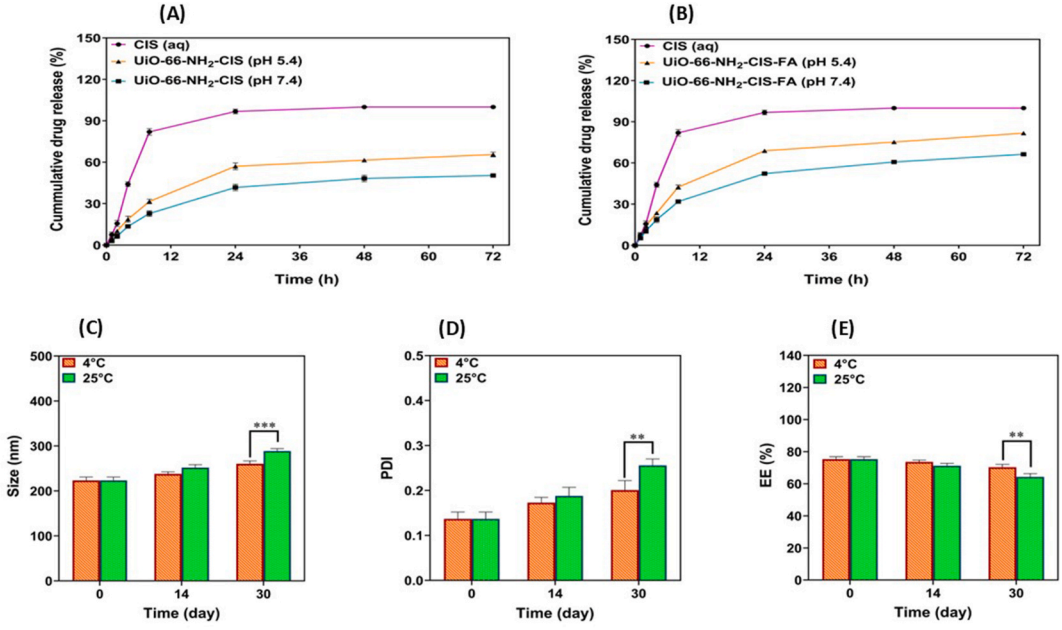

Fig. 2. *In vitro* release of CIS from (A) UiO-66-NH_2-CIS and (B) UiO-66-NH_2-CIS-FA at pH 7.4, and 5.4. The physical stability of UiO-66-NH_2-CIS-FA is based on (C) size, (D) PDI, and (E) EE% at 4 and 25 °C after 30 days (Mean ± SD, n = 3). ***P* < 0.01* and ****P* < 0.001*.

3.2. Drug release and kinetic study

Measuring drug release at different pH levels is crucial, as the extracellular pH is approximately 7.4, whereas the pH within cancerous tissues is around 5.5. This pH gradient provides a potential mechanism for targeted drug delivery. The present study aimed to evaluate the effect of UiO-66-NH_2 and UiO-66-NH_2-FA on CIS release rates and to develop an efficient drug release mechanism through kinetic modeling.

The *in vitro* drug release profiles of UiO-66-NH_2-CIS-FA exhibited a biphasic pattern. During the initial 8 h, a rapid release of 30 % and 45 % was observed at pH 5.4 and 20 % and 30 % at pH 7.4 for UiO-66-NH_2 and its FA-coated form, respectively (Fig. 2A–B). At pH 5.4, UiO-66-NH_2 and UiO-66-NH_2-CIS-FA exhibited cumulative release rates of 70 % and 80 %, respectively, whereas at pH 7.4, the release rates were 50 % and 65 %, respectively.

Fig. 2A–B demonstrate that the release rate of UiO-66-NH_2-CIS-FA increases at lower pH levels (5.4). If this behavior is maintained in biological conditions, UiO-66-NH_2-FA is expected to retain the drug under extracellular conditions, minimizing off-target drug dispersion while facilitating targeted release at the tumor site.

UiO-66, a MOF composed of zirconium-based octahedral clusters coordinated with benzene-1,4-dicarboxylic acid (BDC), undergoes protonation of its carboxylate groups in an acidic environment, leading to structural degradation and enhanced drug release. In addition to pH, various factors, such as ionic intermolecular and intramolecular interactions, hydrogen bonding, and π-π interactions, influence the release of bioactive substances from drug delivery systems [26,54].

Nasrabadi et al. reported a higher ciprofloxacin release of 87 % from UiO-66 at pH 5 compared to 80 % at pH 7.4 after 3 days [26]. Similarly, Chowdhuri et al. found that the release of doxorubicin from UCNP@UiO-66-NH_2/FA increased from 30 % to 40 %–65 % and 72 % at pH 5.5 after 12 and 24 h, respectively [55].

The extensive surface area of UiO-66-NH_2-FA allows for a significant initial release of CIS, which is primarily attributed to the electrostatic interactions between the drug molecules and the MOF surface. The drug release process occurs in two distinct stages: an initial burst release from the outer surface and accessible pores, followed by a sustained release phase involving the diffusion of CIS molecules from the inner pores and cages of the UiO-66-NH_2 structure [30].

The release kinetics of free CIS and UiO-66-NH_2-CIS-FA formulations were analyzed at different pH levels using multiple kinetic models (Table 2). The best-fitting model for each formulation was selected based on the highest correlation coefficient (r^2), which indicates the quality of fit. The data in Table 2 show that the release of free CIS follows a first-order kinetic model, while UiO-66-NH_2-FA formulations exhibit a better fit with the Korsmeyer-Peppas model at both pH 7.4 and 5.4. The n values obtained from the Korsmeyer-Peppas model suggest that CIS release from the MOFs follows a non-Fickian diffusion mechanism at pH 5.4 ($n = 0.55$, $r^2 = 0.9408$) and pH 7.4 ($n = 0.57$, $r^2 = 0.9472$).

3.3. Stability

The physical stability of UiO-66-NH_2-CIS-FA formulations was evaluated over 30 days at two different storage temperatures: ambient temperature (25 °C) and refrigeration (4 °C). Changes in particle size, PDI, and EE% were systematically monitored throughout the study (Fig. 2C, D, and 2E). The formulations stored at 4 °C exhibited minimal changes in particle size and EE%, as illustrated in Fig. 2C, D, and 2E.

However, significant alterations were observed in samples stored at 25 °C. A notable increase in PDI was detected after 30 days ($P < 0.01$), indicating reduced uniformity in particle dispersion. Additionally, a significant increase in particle size ($P < 0.001$) and a decrease in EE% ($P < 0.001$) were recorded compared to samples stored at 4 °C. The observed increase in size and PDI over time may be attributed to particle aggregation, which was more pronounced at 25 °C than at 4 °C.

The decline in EE% during storage suggests gradual drug leakage from the functionalized MOF formulations, which occurred at both temperature conditions but was more prominent at 25 °C. Temperature-induced variations in structural rigidity may also contribute to drug release over time.

UiO-66 was selected as an adsorbent due to its high chemical resistance to polar solvents, including water, various alcohols, and organic solvents, as well as its remarkable thermal stability [56].

3.4. Cytotoxicity

The results of the MTT assay provide a comprehensive understanding of the cellular responses to toxicity. In this study, the

Table 2
The kinetic release models and the parameters obtained for UiO-66-NH_2-CIS-FA.

Kinetic Model	Zero-Order		First-Order	Higuchi	Korsmeyer-Peppas	
	$C_t = C_0 + K_0 t$		$C_t = C_0\, e^{-kt}$ or $\text{Log } C = \text{Log} C_0 - Kt/2.303$	$Q = K_H t^{1/2}$	$M_t/M_\infty = K_{kp} t^n$	
	r^2		r^2	r^2	r^2	n*
CIS (aq)	pH 7.4	0.5698	0.9560	0.7414	0.8195	0.5800
UiO-66-NH_2-CIS-FA	pH 7.4	0.8247	0.9004	0.9444	0.9472	0.5765
	pH 5.4	0.7877	0.9012	0.9197	0.9408	0.5553

anticancer activity of UiO-66-NH_2-CIS-FA was compared with UiO-66-NH_2 and free CIS. UiO-66-NH_2-CIS-FA exhibited significantly higher anticancer efficacy against MDA-MB-231 and A2780 cells. The extent of cytotoxicity induced by UiO-66-NH_2-CIS-FA was dose- and time-dependent, as shown in Fig. 3.

At a concentration of 200 μg/mL, the recorded inhibition rates after 48 h were 51.70 % and 61 % for UiO-66-NH_2-CIS-FA, 50.34 % and 61 % for UiO-66-NH_2-CIS, 42.70 % and 47 % for CIS, and 12 % and 14 % for UiO-66-NH_2 in MDA-MB-231 and A2780 cells, respectively (Fig. 3A–B). After 72 h of treatment at the highest concentration, growth inhibition rates increased to 58 % and 68.34 % for UiO-66-NH_2-CIS-FA, 51.70 % and 59 % for UiO-66-NH_2-CIS, 47 % and 50 % for CIS, and 8.70 % and 14.70 % for UiO-66-NH_2, in MDA-MB-231 and A2780 cells, respectively (Fig. 3C–D).

UiO-66-NH_2-CIS-FA exhibited significantly higher cytotoxicity compared to free CIS after 48 and 72 h of treatment in both cell lines ($P < 0.0001$ and $P < 0.001$, respectively). While the differences between UiO-66-NH_2-CIS-FA and UiO-66-NH_2-CIS in MDA-MB-231 and A2780 cells were minimal, UiO-66-NH_2-CIS-FA induced a more significant reduction in viability in A2780 cells at 200 μg/mL after 72 h ($P < 0.001$).

The results indicate that all treatments exhibited greater cytotoxic effects against A2780 cells compared to MDA-MB-231 cells. The enhanced cytotoxicity of CIS-loaded UiO-66-NH_2 and UiO-66-NH_2-FA compared to free CIS suggests improved cellular uptake and intracellular accumulation, leading to cellular stress and apoptosis [57]. The cytotoxic effects of functionalized MOFs may be attributed to the upregulation of pro-apoptotic BAX, a member of the BCL2 family, which promotes mitochondrial outer membrane permeabilization and the release of soluble pro-apoptotic proteins into the cytoplasm, ultimately activating the intrinsic apoptotic pathway [58]. The lower sensitivity of MDA-MB-231 cells to treatment may be associated with the lack of HER_2 amplification, estrogen receptor (ER), and progesterone receptor (PR) expression, as well as alterations in multidrug resistance (MDR) gene expression [59].

The MTT assay results for HFF cells indicated that UiO-66-NH_2-CIS-FA exhibited lower cytotoxicity toward normal cells compared to UiO-66-NH_2-CIS and free CIS at both tested time points (Fig. 3E–F). The incorporation of CIS into the UiO-66-NH_2-FA framework effectively reduced its harmful effects on healthy cells. The highest tested concentration of UiO-66-NH_2-CIS-FA (200 μg/mL) resulted in 80.66 % and 76.66 % cell viability in HFF cells after 48 and 72 h of treatment, respectively. These findings demonstrate that cancer cells exhibited significantly higher sensitivity to UiO-66-NH_2-CIS-FA compared to normal HFF cells.

The IC_{50} values of UiO-66-NH_2-CIS-FA were determined to be 144.8 ± 5.6 μg/mL for MDA-MB-231 cells and 75.43 ± 2.8 μg/mL for A2780 cells after 48 h of exposure. Following 72 h of treatment, the IC_{50} values decreased to 116.33 ± 2.84 μg/mL and 37.52 ± 2.8 μg/mL for MDA-MB-231 and A2780 cells, respectively.

In contrast, the IC_{50} values of free CIS for MDA-MB-231 and A2780 cells were 166.07 ± 2.38 μg/mL and 163.33 ± 2.6 μg/mL, respectively, after 48 h of exposure. After 72 h, the IC_{50} values of CIS were estimated at 131.38 ± 1.5 μg/mL for MDA-MB-231 cells and

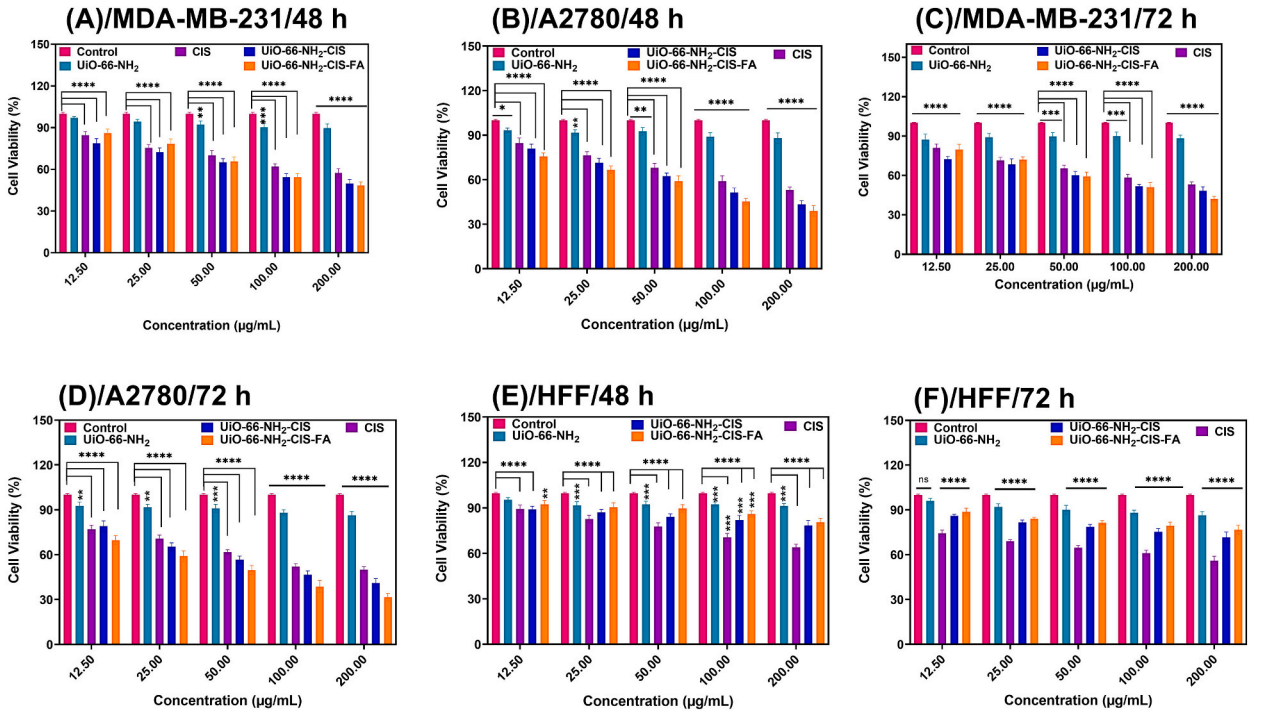

Fig. 3. (A, B) MDA-MB-231 and A2780 cells viability upon exposure to different concentrations of CIS, UiO-66-NH_2, UiO-66-NH_2-CIS, and UiO-66-NH_2-CIS-FA after 48 h of treatment. (C, D) MDA-MB-231 and A2780 cells viability upon exposure to different concentrations of CIS, UiO-66-NH_2, UiO-66-NH2-CIS, and UiO-66-NH_2-CIS-FA after 72 h of treatment. (E, F) HFF cells viability upon exposure to different concentrations of CIS, UiO-66-NH_2, UiO-66-NH_2-CIS, and UiO-66-NH_2-CIS-FA in 48 and 72 h. Data represent means ± standard deviations (SD)(n = 3). Statistical comparisons were performed relative to the control group. For all charts, *: $P < 0.05$, **: $P < 0.01$, ***: $P < 0.001$, and ****: $P < 0.0001$, ns: non-significant.

129.84 ± 2.74 μg/mL for A2780 cells.

A notable reduction in the IC_{50} values of UiO-66-NH_2-CIS-FA compared to free CIS was observed in both cancer cell lines following 48- and 72-h treatments, indicating the enhanced anticancer efficacy of the nanocarrier system.

Cancer targeting represents an innovative, promising, and efficient strategy in cancer biotherapy. UiO-66-NH_2 has demonstrated significant potential as a drug delivery carrier due to its unique structural properties and functionalization capabilities. The amine-functionalized UiO-66-NH_2 has been widely investigated for its role in enhancing the delivery and therapeutic efficacy of various anticancer agents, yielding promising outcomes in multiple cancer models [60].

Hashemzadeh et al. utilized magnetic UiO-66-NH_2 (MU) loaded with oxaliplatin (OX) to improve its therapeutic efficacy. The results demonstrated a significant enhancement in anticancer activity compared to free OX, as evaluated in both two-dimensional and three-dimensional colorectal cancer models. Parameters such as cell viability, proliferation, migration, and morphology were assessed, indicating the superior performance of the developed drug delivery system. Moreover, the oxidative and antioxidant activities of UiO-66-NH_2 and MU-loaded OX exhibited enhanced oxidative effects relative to OX alone [29].

UiO-66-NH_2 MOFs have also shown considerable potential in anticancer applications as carriers for doxorubicin. Studies have demonstrated that doxorubicin-loaded UiO-66-NH_2 MOFs exhibit high biocompatibility, maintaining cell viability above 90 % in normal fibroblast L929 cells [30]. Gholamie et al. investigated a novel drug delivery system, 5-FU@CuS/NH_2-UiO-66, which incorporates copper sulfide nanoparticles to enhance the antiproliferative effects of 5-fluorouracil (5-FU) against colorectal cancer cells. The integration of CuS nanoparticles into the UiO-66-NH_2 structure resulted in improved therapeutic outcomes [61].

In another study, OXA-CuS@UiO-66-NH_2 was employed for colorectal cancer treatment. The IC_{50} value for OXA-CuS@UiO-66-NH_2 was determined to be 7.97 ppm, significantly lower than that of free oxaliplatin, indicating enhanced cytotoxicity and therapeutic efficacy [62].

Furthermore, the UiO-66-NH_2 nanoparticle loaded with temozolomide (TMZ) exhibited enhanced antitumor efficacy against malignant glioma. The study demonstrated that TMZ@UiO-66-NH_2 nanocomposites, particularly when combined with ultrasound,

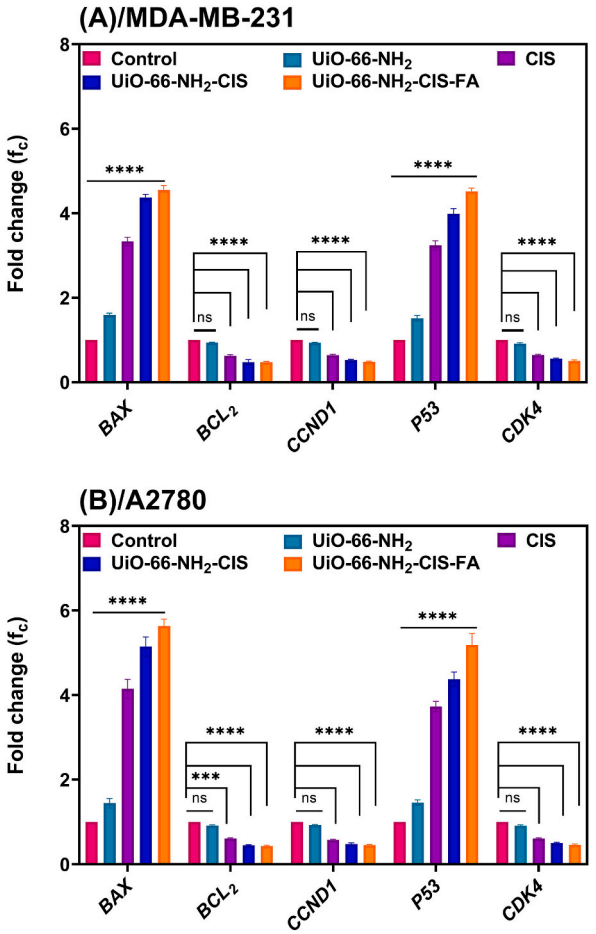

Fig. 4. The expression level of *BAX, BCL2, CCND1, P53,* and *CDK4* genes in (A) MDA-MB-231 and (B) A2780 cell lines upon exposure to IC_{50} concentrations of UiO-66-NH_2, CIS, UiO-66-NH_2-CIS, and UiO-66-NH_2-CIS-FA after 48 h of treatment. Data represent means ± SD (n = 3). Statistical comparisons were performed relative to the control group. For all charts, ***: $P < 0.001$ and ****: $P < 0.0001$, ns: non-significant.

significantly inhibited tumor growth compared to TMZ alone [63].

The study conducted by Lázaro evaluated the anticancer efficacy of dichloroacetate-loaded UiO-66 nanoparticles coated with various functional materials, including FA, polyethylene glycol (PEG), poly-l-lactide, and poly-N-isopropylacrylamide, in MCF-7 breast cancer cells and HEK293 healthy kidney cells. The *in vitro* results demonstrated that FA-modified UiO-66 preferentially eliminated cancer cells while sparing healthy cells and avoiding immune system activation. These findings highlight the targeted nature of FA-functionalized MOFs and their potential in developing efficient anticancer drug delivery systems [64]. The enhanced targeting efficiency of FA-modified MOFs is attributed to the strong affinity of FA for folate receptors overexpressed on the surface of cancer cells, facilitating efficient cellular uptake and accelerated cell death [65].

In a study by Hashemzadeh et al., the efficacy of a UiO-66-NH_2-based oxaliplatin delivery system was evaluated using the MTT assay on CT-26 colorectal cancer cells. The IC_{50} values were determined to be 21.38, 95.50, and 18.20 μg/mL for oxaliplatin, UiO-66-NH_2-oxaliplatin, and UiO-66-NH_2-oxaliplatin@FA, respectively, indicating a significant enhancement in cytotoxicity upon FA functionalization [66].

Trucshina et al. compared the cytotoxic effects of doxorubicin-loaded UiO-66@SiO_2 and UiO-66@SiO_2@pluronic F127-FA nanoparticles in MCF-7 cells. Their findings revealed that the SiO_2 shell and pluronic F127-FA-modified nanoparticles exhibited superior toxicity at all tested doxorubicin concentrations after 24 and 72 h of treatment. This increased toxicity was attributed to the enhanced cellular uptake facilitated by folate receptor-mediated endocytosis [23]. In another study, Soman et al. demonstrated that the IC_{50} value of UiO-doxorubicin@chitosan-FA (0.085 μg/mL) was lower compared to free doxorubicin (0.28 μg/mL) and UiO-doxorubicin (0.13 μg/mL), further supporting the role of FA functionalization in enhancing drug delivery efficacy via receptor-mediated uptake [36].

These findings align with the current study, further validating that FA-functionalized MOFs enhance the cytotoxic effects of loaded drugs by improving targeted delivery and cellular uptake mechanisms.

3.5. Real-time PCR findings

The expression levels of *BAX, BCL2, CCND1, P53,* and *CDK4* genes were evaluated in MDA-MB-231 and A2780 cancer cells treated with different formulations using RT-qPCR. Fig. 4A presents the results for MDA-MB-231 cells, while Fig. 4B displays the findings for A2780 cells.

A comparison of gene expression levels between treated cancer cells and the control group revealed a significant upregulation of the pro-apoptotic genes *BAX* and *P53* ($P < 0.001$) (Fig. 4A–B), along with a notable downregulation of the anti-apoptotic *BCL2* and the cell cycle-related genes *CCND1* and *CDK4* after 48 h of exposure to CIS, UiO-66-NH_2-CIS, and UiO-66-NH_2-CIS-FA formulations ($P < 0.001$).

Furthermore, treatment with UiO-66-NH_2-CIS-FA resulted in significantly higher expression levels of *BAX* and *P53* in both cell lines compared to CIS or UiO-66-NH_2-CIS alone ($P < 0.001$). However, no significant differences were observed in the expression levels of *BCL2, CCND1,* and *CDK4* among cells treated with CIS, UiO-66-NH_2-CIS, and UiO-66-NH_2-CIS-FA.

These findings support the observed cytotoxic effects of the formulations, which were confirmed by the modulation of apoptotic and cell cycle-related gene expression. The results are consistent with the MTT assay outcomes, further validating the enhanced anticancer efficacy of the functionalized MOFs.

The apoptotic process is highly complex and challenging to quantify due to interactions among numerous biological pathways. Several genes, including *BCL2* and *BAX*, play critical roles in apoptosis, with a particular focus on the *BCL2* family. Studies have demonstrated that the BCL2 family members can both inhibit and promote apoptosis, influencing the balance between programmed cell death and cell proliferation [67]. BAX, in association with BCL2, functions as a pro-apoptotic factor by promoting programmed cell death when overexpressed in response to apoptotic signals. Conversely, BCL2 suppresses apoptosis by forming heterodimers with BAX, thereby inhibiting cell death [68].

P53 plays an essential role in cell cycle regulation, apoptosis, and genomic stability maintenance. The protein product of *P53* acts as a tumor suppressor by initiating transcription, binding to DNA, and forming oligomers. It regulates the expression of target genes in response to cellular stress, leading to outcomes such as cell cycle arrest, apoptosis, senescence, DNA repair, and metabolic adaptations [69]. Due to its pivotal role in preventing genetic mutations and maintaining genomic integrity, *P53* is often referred to as "the guardian of the genome." However, excessive *P53* expression may accelerate aging by inducing excessive apoptosis while simultaneously suppressing tumor growth [70].

The findings suggest that the synthesized formulations induce apoptosis in cancer cells by upregulating *BAX* and *P53* expression while downregulating the anti-apoptotic *BCL2* gene. This modulation of gene expression represents a potential molecular mechanism underlying the cytotoxic effects of the prepared formulations.

Cyclins are regulatory proteins that control cell cycle progression by activating cyclin-dependent kinases (CDKs). CDK4/6 is critical in the G1-to-S phase transition of the cell cycle. Growth factors often activate the mitogen-activated protein kinase (MAPK) pathway during the G1 phase, leading to the transcription of cyclin D genes, which subsequently bind to and activate CDK4 and CDK6 [71]. The internalization of the prepared nanocarriers into cancer cells can induce DNA damage, resulting in irreversible cell cycle arrest at various stages. This process is closely linked to the activation of apoptotic pathways [72].

Consistent with the findings of this study, UiO-66 loaded with gingerol (Gin) has been shown to upregulate the expression of pro-apoptotic genes, including *BAX, CASP3*, and *CASP9*, while downregulating the expression of *BCL2* in AGS gastric cancer cells compared to Gin alone [73]. Similarly, Bazzazan et al. demonstrated that the incorporation of curcumin into UiO-66 significantly enhanced its anticancer efficacy. Specifically, UiO-66-curcumin effectively induced *CASP3* and *CASP9* expression while suppressing the production of *MMP-2*, *MMP-9*, and cyclin E/D in cancer cell lines, as confirmed by RT-qPCR analysis [20].

3.6. Apoptotic study

Flow cytometry analysis was conducted to evaluate cytotoxicity, apoptosis, and necrosis in MDA-MB-231 and A2780 cancer cells treated with different formulations, including UiO-66-NH_2, CIS, UiO-66-NH_2-CIS, and UiO-66-NH_2-CIS-FA (Fig. 5). The cells were exposed to these formulations at their respective IC_{50} concentrations for 48 h.

The results indicated that UiO-66-NH_2 alone did not significantly impact apoptosis or necrosis rates in cancer cells compared to the control group. As shown in Fig. 5A–B, the apoptosis rate in MDA-MB-231 and A2780 cells treated with CIS was approximately 1.85 % (0.12 % early apoptosis and 1.73 % late apoptosis) and 2.49 % (2.61 % early apoptosis and 2.36 % late apoptosis), respectively.

In contrast, treatment with UiO-66-NH_2-CIS resulted in a marked increase in apoptosis, with rates of 38.45 % (13.95 % early apoptosis and 21.35 % late apoptosis) for MDA-MB-231 cells and 42.01 % (34.05 % early apoptosis and 7.96 % late apoptosis) for A2780 cells. The highest apoptotic rates were observed in cells treated with UiO-66-NH_2-CIS-FA, reaching 44.75 % (27.05 % early apoptosis and 17.7 % late apoptosis) in MDA-MB-231 cells and 54.48 % (44.70 % early apoptosis and 9.78 % late apoptosis) in A2780 cells.

Apoptosis rates in cells treated with UiO-66-NH_2-CIS and UiO-66-NH_2-CIS-FA were significantly higher than those observed in cells treated with CIS or the control group ($P < 0.001$). Among the tested formulations, UiO-66-NH_2-CIS-FA demonstrated the most pronounced apoptotic effect.

Although CIS induced substantial necrosis in both MDA-MB-231 and A2780 cells, its incorporation into UiO-66-NH_2 and UiO-66-NH_2-FA formulations significantly reduced the necrotic effect while enhancing apoptosis ($P < 0.001$) (Fig. 5C for MDA-MB-231 and Fig. 5D for A2780 cells).

Flow cytometry is a rapid and precise method for assessing apoptosis and quantifying apoptotic rates. This technique provides a practical and efficient approach for evaluating the effectiveness of pharmaceuticals and nanodrugs, serving as a reliable tool for the

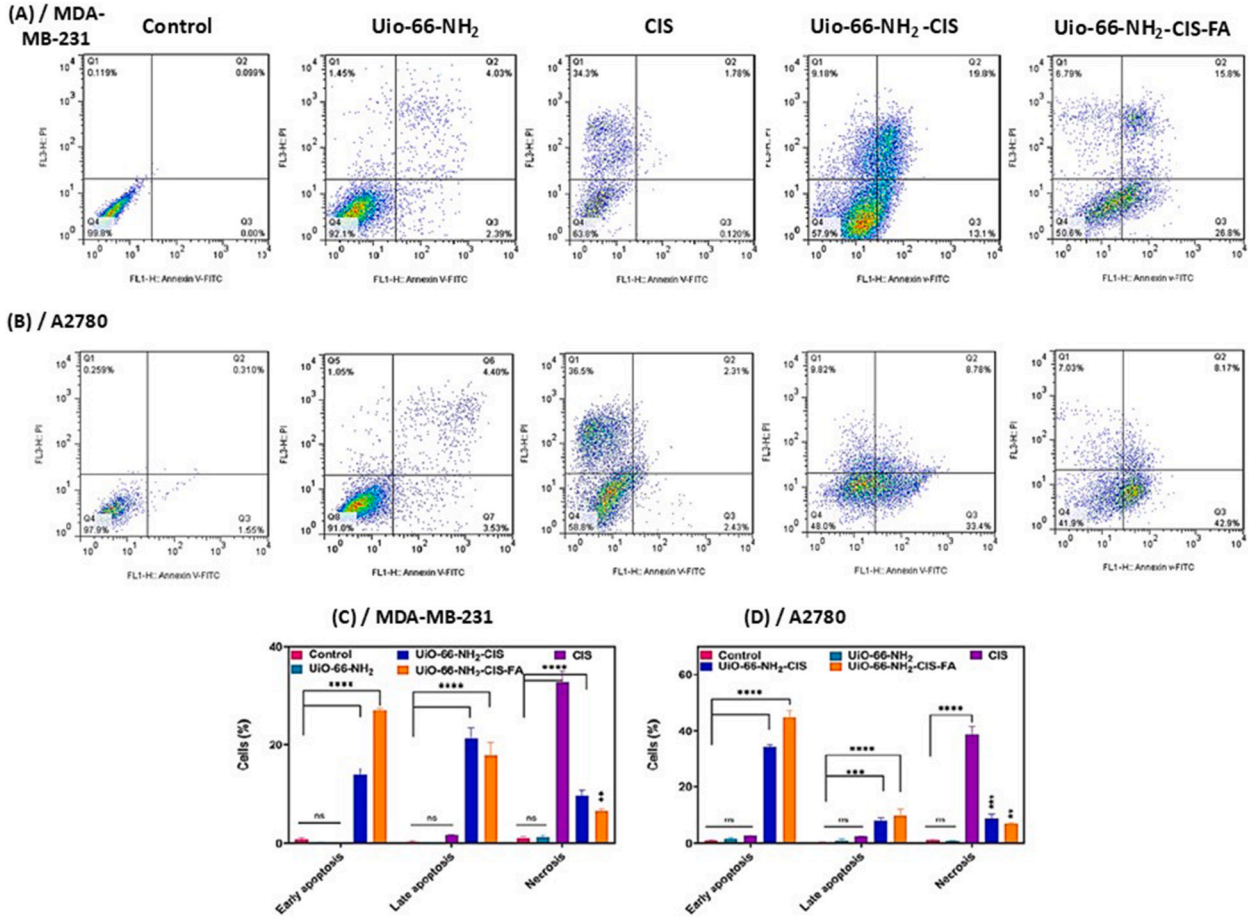

Fig. 5. (A, B) Flow cytometry analysis diagrams of (A) MDA-MB-231, and (B) A2780 cells treated with UiO-66-NH_2, CIS, UiO-66-NH_2-CIS, UiO-66-NH2-CIS-FA. Q1 shows the percentage of necrotic cells, Q2 exhibits the percentage of late apoptotic cells, Q3 exhibits the percentage of early apoptotic cells, and Q4 shows the percentage of live cells. (C, D) The apoptosis rates (%) following treatment by UiO-66-NH_2, CIS, UiO-66-NH_2-CIS, UiO-66-NH_2-CIS-FA on (C) MDA-MB-231, and (D) A2780 cells. The IC_{50} was used for each sample; Data represent means ± SD (n = 2). Statistical comparisons were performed relative to the control group. For all charts, ***: $P < 0.01$, ***: $P < 0.001$,* and ****: $P < 0.0001$, ns: non-significant.

identification of apoptotic cells [49]. Accordingly, the apoptosis rate in the current study was assessed using flow cytometry [74]. The flow cytometry results demonstrated that UiO-66-NH_2-CIS-FA exhibited more significant cytotoxic activity against A2780 cells compared to MDA-MB-231 cells. The primary mechanism through which CIS exerts its cytotoxic effects involves the formation of adducts with gDNA. More specifically, initial interactions at the plasma membrane (PM), including the binding of platinum to membrane components, contribute to cellular uptake and cytotoxicity. Structural and flexibility changes in the cell membrane induced by CIS have been shown to activate signaling pathways that lead to programmed cell death [75]. In line with these findings, Ashrafi et al. reported that the apoptosis rate in *AGS* cells treated with UiO-66-Gin was significantly higher than in cells treated with Gin alone, as confirmed by flow cytometry analysis [73]. Furthermore, the internalization of quercetin@Fe_3O_4-COOH@UiO-66-NH_2 by breast cancer cells was shown to induce apoptosis, highlighting the potential of functionalized UiO-66-NH_2 for targeted cancer therapy [27].

Ronaghi et al. demonstrated that letrozole-loaded UiO-66 nanoparticles significantly enhanced the cytotoxic effects of letrozole compared to its free form, effectively promoting apoptosis and inhibiting cancer cell migration [47]. Similarly, Bazzazan et al. reported that their flow cytometry analysis revealed a significant increase in apoptosis in breast cancer cells treated with UiO-66-curcumin at IC_{50} concentrations. Notably, UiO-66-curcumin demonstrated a substantial capacity to induce apoptosis in both MDA-MB-231 and SKBR3 cells compared to curcumin alone [20].

CIS is a platinum-based chemotherapy drug that interacts with DNA, causing damage that ultimately leads to cell death. It forms inter- and intra-strand adducts, primarily between guanine and adenine nucleobases within DNA strands. Initially, CIS binds to the *N7* position of guanine, followed by a second bond formation with either guanine or adenine on the same or opposite DNA strand. The accessibility of *N7* atoms enables the formation of multiple adducts and cross-links, leading to DNA structural distortion [76,77].

As a result of CIS binding, DNA undergoes bending, which is recognized by high-mobility group (HMG) proteins. These proteins shield the distorted DNA from repair mechanisms such as nucleotide excision repair (NER) and mismatch repair (MMR), thereby preventing damage reversal. This process triggers the activation of P53, a crucial tumor suppressor protein responsible for maintaining genomic integrity. The activation of P53 leads to the upregulation of downstream effector proteins, such as waf1, P21, and MDM2,

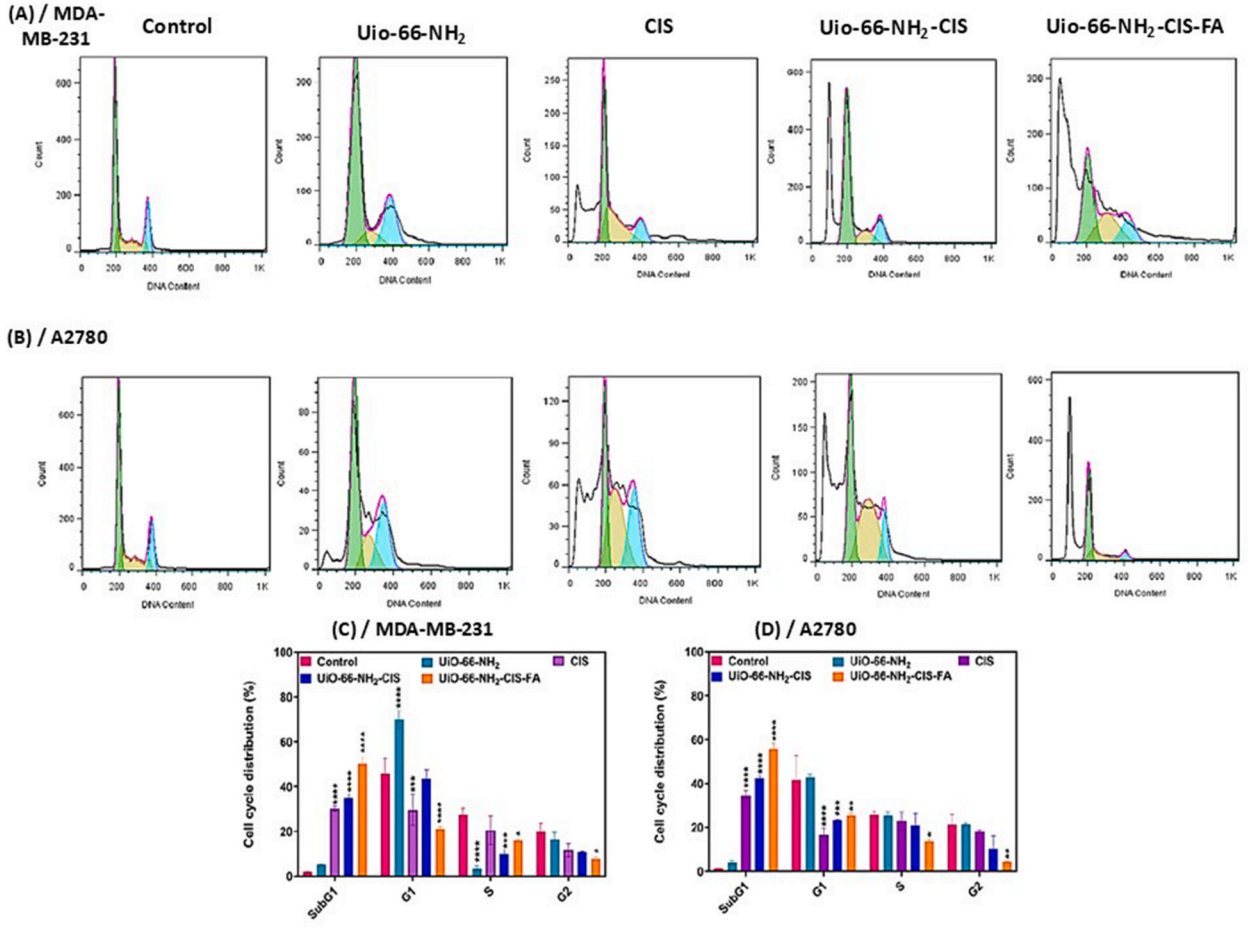

Fig. 6. (A, B) Cell cycle analysis diagrams of UiO-66-NH_2, CIS, UiO-66-NH_2-CIS, UiO-66-NH_2-CIS-FA treated (A) MDA-MB-231, and (B) A2780 cells. (C, D) The cell cycle distribution (%) of UiO-66-NH_2, CIS, UiO-66-NH_2-CIS, UiO-66-NH_2-CIS-FA treated (C) MDA-MB-231, and (D) A2780 cells. IC_{50} concentration was used for each sample; Data represent means ± SD (n = 2). Statistical comparisons were performed relative to the control group. For all charts, **: $P < 0.05$, **: $P < 0.01$, ***: $P < 0.001$,* and *****: $P < 0.0001$.*

which induce cell cycle arrest [78,79].

In addition to DNA damage, CIS induces oxidative stress by generating ROS, which damages cellular components, including DNA, proteins, and lipids. When the damage surpasses the cell's repair capacity, the intrinsic apoptotic pathway is activated. This involves the inhibition of BCL2, which compromises mitochondrial membrane integrity. CIS also depletes mitochondrial glutathione levels, exacerbating oxidative stress and further destabilizing the mitochondrial membrane [80–82].

As a consequence of mitochondrial dysfunction, cytochrome *C* is released into the cytoplasm, where it interacts with apoptotic protease-activating factor-1 (Apaf-1), leading to the activation of procaspase-9. This cascade further activates executioner caspases, including caspase-3 and caspase-7, which cleave and activate poly (ADP-ribose) polymerase (PARP), ultimately resulting in apoptosis through DNA fragmentation and degradation of key cellular proteins [83–85].

CIS preferentially targets mitochondrial DNA (mtDNA) due to its high guanine content, forming adducts more frequently in mtDNA than in nuclear DNA. This specificity suggests that mitochondrial functions, crucial for energy production and other cellular processes, are severely disrupted by CIS treatment, contributing to its cytotoxic effects [86].

In cancer cells such as MDA-MB-231 and A2780, folate receptor expression on the cell membrane is significantly elevated compared to normal cells. This overexpression facilitates the precise targeting of FA-modified nanoparticles to tumor sites through receptor-mediated endocytosis [87]. Upon internalization, CIS encapsulated within UiO-66-NH_2-FA is released intracellularly in response to the acidic tumor microenvironment, which triggers the acid-responsive MOF structure. The FA moiety serves as a tumour-specific targeting ligand, enabling selective drug delivery and minimizing off-target effects.

The developed FA-functionalized nanoformulation combines both targeting specificity and stimuli-responsive release, leading to selective cytotoxic effects in MDA-MB-231 and A2780 cells while sparing normal cells. In conclusion, the UiO-66-NH_2-FA nanocarrier demonstrated superior targeting and cytotoxicity compared to free CIS, highlighting its potential as an effective cancer treatment strategy.

3.7. Cell cycle study

The impact of CIS, UiO-66-NH_2, UiO-66-NH_2-CIS, and UiO-66-NH_2-CIS-FA on cell cycle progression in MDA-MB-231 and A2780 cancer cells was evaluated using flow cytometry (Fig. 6A–B). As shown in Fig. 6C–D, treatment with CIS, UiO-66-NH_2-CIS, and UiO-66-NH_2-CIS-FA significantly inhibited cell growth by inducing cell cycle arrest in the sub-G1 phase in both cell lines compared to the control group ($P < 0.001$).

In MDA-MB-231 cells, the sub-G1 phase population following treatment with CIS, UiO-66-NH_2-CIS, and UiO-66-NH_2-CIS-FA was approximately 30.18 %, 34.91 %, and 50.29 %, respectively. Similarly, in A2780 cells, the sub-G1 phase population was approximately 35 %, 42.31 %, and 55.59 %, respectively.

Treatment with UiO-66-NH_2-CIS-FA led to a reduction in the proportion of cells in the S phase (15.82 % in MDA-MB-231 and 14.31 % in A2780 cells) and G2 phase (7.57 % in MDA-MB-231 and 4.16 % in A2780 cells). These results align with the apoptosis assay findings, which demonstrated a higher apoptosis rate and cell cycle arrest in the sub-G1 phase, particularly in A2780 cells treated with UiO-66-NH_2-CIS-FA. Additionally, RT-qPCR results confirmed that cell cycle arrest in the sub-G1 phase correlated with the down-regulation of *CCND1* and *CDK4* gene expression.

The sub-G1 phase represents the proportion of cancer cells undergoing apoptosis [88]. The findings of this study suggest that MOF nanocomposites have the potential to serve as effective drug delivery systems, owing to their high drug-loading capacity and controlled release properties [11]. The primary objective of novel nanomaterials in cancer treatment is to enhance therapeutic efficacy through targeted drug delivery, which can be more effective than conventional methods.

Nanomaterials present a promising strategy to overcome the limitations of traditional cancer therapies and diagnostics by enabling targeted treatment of circulating cancer cells in the bloodstream [89]. Previous studies on cell cycle analysis have shown that treatment with CIS can induce cell cycle arrest in the sub-G1 phase across various cancer cell lines [40,90–93]. This accumulation in the sub-G1 phase is primarily attributed to defects in DNA repair mechanisms, which prevent damaged cells from progressing through the cell cycle [94].

Furthermore, a study investigating the effects of curcumin and UiO-66-curcumin at IC_{50} concentrations on breast cancer cells demonstrated a significant increase in the sub-G1 cell population. This increase was more pronounced compared to the control and UiO-66-treated groups, indicating enhanced apoptotic effects [20].

Additionally, it has been reported that other MOFs, such as MOF-74 (Co) [95] and ultra-small Ti-tetrakis (4-carboxyphenyl) porphyrin MOF, are capable of inducing cell cycle arrest in the sub-G1 phase in various cancer cell lines, further supporting the potential of MOFs as effective platforms for cancer treatment [95].

3.8. ROS generation in treated cells

Oxidative stress is a critical factor contributing to tumor cell death. While a moderate increase in ROS facilitates cellular proliferation, excessive ROS levels trigger apoptosis [96]. In this study, ROS production was quantified using DCFDA, which is oxidized inside cells to form the fluorescent compound DCF. ROS generation in MDA-MB-231 and A2780 cells was measured following treatment with IC_{50} concentrations of UiO-66-NH_2, CIS, UiO-66-NH_2-CIS, and UiO-66-NH_2-CIS-FA (Fig. 7A–B).

No significant changes in ROS production were observed in cells treated with UiO-66-NH_2 compared to the control group. However, significant increases in DCF fluorescence were detected in cells treated with CIS, UiO-66-NH_2-CIS, and UiO-66-NH_2-CIS-FA compared to the control group ($P < 0.001$). The intracellular ROS levels in MDA-MB-231 and A2780 cells treated with UiO-66-NH_2-CIS-FA at IC_{50}

concentrations were 2977.5 % and 3500.5 %, respectively, demonstrating the highest ROS generation among all groups.

Previous studies have suggested that MOFs possess potential as novel disinfectants due to their ability to generate ROS through photocatalytic activity. This ROS-generating capacity positions MOFs as promising carriers for chemotherapeutic agents [97–99].

It is well established that excessive ROS levels result in cellular damage by causing oxidative stress to DNA, proteins, and lipids [100]. High ROS concentrations can alter protein function by modulating redox-sensitive proteins, influencing gene expression, modifying redox-sensitive enzymes, and regulating protein turnover. Cancer cells typically exhibit higher basal levels of ROS than normal cells due to factors such as hypoxia, genetic mutations in nuclear and mitochondrial DNA, oncogene activation, and loss of tumor suppressor genes [101]. While cancer cells rely on low to moderate ROS levels for key processes such as cell growth, differentiation, and survival, excessive ROS levels can lead to apoptotic cell death. Emerging evidence suggests that ROS play a crucial role as signaling molecules in tumor cell invasion, angiogenesis, and metastasis [102].

Consistent with these findings, Hashemzadeh et al. demonstrated that UiO-66-Oxaliplatin-FA induced more outstanding ROS production and disrupted the antioxidant defence system more effectively than UiO-66-Oxaliplatin or the free drug alone [66].

3.9. Limitations of the study

A comprehensive understanding of the specific anticancer effects of UiO-66-NH_2-CIS-FA requires further investigation through *in vivo* and clinical studies. The most effective approach to evaluating drug delivery systems involves a combination of *in vitro, in vivo,* and clinical trials. Initial screening in cell culture serves as a critical preliminary step, enabling the selection of the most promising formulation for subsequent testing in animal models. Following successful preclinical evaluation, the optimized formulation can be advanced to clinical trials for further validation of its therapeutic efficacy and safety in humans.

4. Conclusion

UiO-66-NH_2 nanocomposites demonstrate significant potential as anticancer agents due to their unique physicochemical properties and mechanisms of action. The high surface area, tunable pore size, biocompatibility, and chemical stability of these nanoparticles provide a promising platform for targeted drug delivery and combination therapy. Their pH-responsive behavior, enhanced drug release capabilities, and exploitation of the enhanced permeability and retention (EPR) effect position UiO-66-NH_2 as a valuable tool in cancer treatment. By leveraging nanotechnology, UiO-66-NH_2 nanoparticles represent a cutting-edge approach, offering the potential for more effective and personalized cancer therapies.

This study introduces a novel FA-functionalized UiO-66-NH_2 MOF for targeted CIS delivery. The incorporation of FA significantly improves the selective delivery of CIS to MDA-MB-231 breast cancer and A2780 ovarian cancer cells. The developed system exhibits a pH-responsive release profile, ensuring optimal drug release in the acidic tumor microenvironment. Compared to free CIS, the synthesized UiO-66-NH_2-CIS-FA formulation demonstrated enhanced anticancer efficacy.

Comprehensive *in vitro* analyses revealed that UiO-66-NH_2-CIS-FA induces apoptosis and cell cycle arrest by upregulating pro-apoptotic genes (*BAX, P53*) and downregulating anti-apoptotic and proliferative markers (*BCL2, CCND1, CDK4*). These findings establish FA-decorated UiO-66-NH_2-CIS as a promising targeted nanocarrier, offering improved cytotoxicity and selectivity against cancer cells while maintaining biocompatibility with healthy cells.

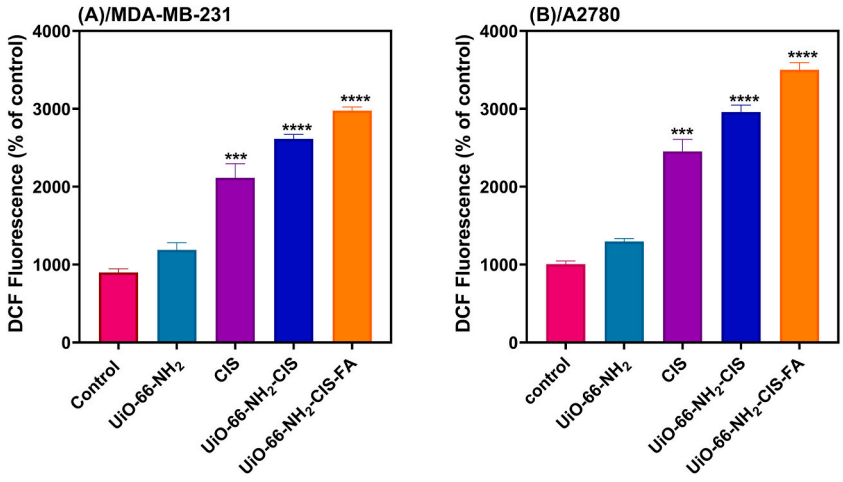

Fig. 7. The ROS generation in (A) MDA-MB-231 and (B) A2780 cell lines upon exposure to IC_{50} concentrations of UiO-66-NH_2, CIS, UiO-66-NH_2-CIS, and UiO-66-NH_2-CIS-FA after 48 h of treatment. Data represent means ± SD (n = 3). Statistical comparisons were performed relative to the control group. For all charts, ***: $P < 0.001$, and ****: $P < 0.0001$.

CRediT authorship contribution statement

Zahra Sadeghi Jam: Writing – original draft, Methodology, Investigation, Formal analysis, Data curation. **Farzaneh Tafvizi:** Writing – review & editing, Supervision, Project administration, Methodology, Investigation, Formal analysis, Data curation. **Parvin Khodarahmi:** Methodology. **Parvaneh Jafari:** Methodology. **Fahimeh Baghbani-Arani:** Methodology.

Data availability

The data used to support the findings of this study are available from the corresponding author upon request.

Funding source

No funding.

Declaration of competing interest

The authors declare that they have no known competing financial interests or personal relationships that could have appeared to influence the work reported in this paper.

Acknowledgment

The authors would like to acknowledge the laboratory of Islamic Azad University.

References

[1] H. Sung, J. Ferlay, R.L. Siegel, M. Laversanne, I. Soerjomataram, A. Jemal, F. Bray, Global cancer statistics 2020: GLOBOCAN estimates of incidence and mortality worldwide for 36 cancers in 185 countries, CA Cancer J. Clin. 71 (3) (2021) 209–249.
[2] A.T. Ali, O. Al-Ani, F. Al-Ani, Epidemiology and risk factors for ovarian cancer, Prz Menopauzalny 22 (2) (2023) 93–104.
[3] S. Łukasiewicz, M. Czeczelewski, A. Forma, J. Baj, R. Sitarz, A. Stanisławek, Breast cancer—epidemiology, risk factors, classification, prognostic markers, and current treatment strategies—an updated review, Cancers 13 (17) (2021) 4287.
[4] K. Grabska, I. Pilarska, M.M. Fudalej, A. Deptała, A. Badowska-Kozakiewicz, What is new about ovarian malignancies? Contemporary Oncology/Współczesna Onkologia 25 (4) (2021) 225–231.
[5] A. Gelasco, S.J. Lippard, Anticancer activity of cisplatin and related complexes. Metallopharmaceuticals I, DNA Interactions (1999) 1–43.
[6] M. Kanamala, W.R. Wilson, M. Yang, B.D. Palmer, Z. Wu, Mechanisms and biomaterials in pH-responsive tumour targeted drug delivery: a review, Biomaterials 85 (2016) 152–167.
[7] S. Ghosh, Cisplatin: the first metal based anticancer drug, Bioorg. Chem. 88 (2019) 102925.
[8] M. Li, Z. Tang, Y. Zhang, S. Lv, Q. Li, X. Chen, Targeted delivery of cisplatin by LHRH-peptide conjugated dextran nanoparticles suppresses breast cancer growth and metastasis, Acta Biomater. 18 (2015) 132–143.
[9] J.K. Patra, G. Das, L.F. Fraceto, E.V.R. Campos, MdP. Rodriguez-Torres, L.S. Acosta-Torres, et al., Nano based drug delivery systems: recent developments and future prospects, J. Nanobiotechnol. 16 (2018) 1–33.
[10] H. Iinuma, K. Maruyama, K. Okinaga, K. Sasaki, T. Sekine, O. Ishida, et al., Intracellular targeting therapy of cisplatin-encapsulated transferrin-polyethylene glycol liposome on peritoneal dissemination of gastric cancer, Int. J. Cancer 99 (1) (2002) 130–137.
[11] M.X. Wu, Y.W. Yang, Metal–organic framework (MOF)-based drug/cargo delivery and cancer therapy, Adv. Mater. 29 (23) (2017) 1606134.
[12] S. Sajjadifar, F. Abakhsh, Z. Arzehgar, Design and characterization of Fe_3O_4@ n-pr-NH_2@ Zn_3 (BTC) $_2$ magnetic MOF: a Catalyst for Dihydropyrimidine and 2-Amino-4H-Chromene synthesis, Chem Methodologies 8 (2024) 550–568.
[13] B.F. Hoskins, R. Robson, Infinite polymeric frameworks consisting of three dimensionally linked rod-like segments, J. Am. Chem. Soc. 111 (15) (1989) 5962–5964.
[14] N. Zhang, Y. Xie, Y. Tai, Y. Gao, W. Guo, W. Yu, et al., Bufalin inhibits hTERT expression and colorectal cancer cell growth by targeting CPSF4, Cell. Physiol. Biochem. 40 (6) (2016) 1559–1569.
[15] A. Amiri, F. Ghaemi, B. Maleki, Hybrid nanocomposites prepared from a metal-organic framework of type MOF-199 (Cu) and graphene or fullerene as sorbents for dispersive solid phase extraction of polycyclic aromatic hydrocarbons, Microchim. Acta 186 (2019) 1–8.
[16] H. Zeng, C. Xia, B. Zhao, M. Zhu, Folic acid–functionalized metal-organic framework nanoparticles as drug carriers improved bufalin antitumor activity against breast cancer, Front. Pharmacol. 12 (2022) 747992.
[17] S. Ibrar, N.Z. Ali, E.O. Ojegu, O.B. Odia, I. Ikhioya, I. Ahmad, Assessing high-performance energy storage of the synthesized ZIF-8 and ZIF-67, Journal of Applied Organometallic Chemistry 3 (4) (2023) 294–307.
[18] F. Vermoortele, B. Bueken, G. Le Bars, B. Van de Voorde, M. Vandichel, K. Houthoofd, et al., Synthesis modulation as a tool to increase the catalytic activity of metal–organic frameworks: the unique case of UiO-66 (Zr), J. Am. Chem. Soc. 135 (31) (2013) 11465–11468.
[19] R.T. Jerozal, T.A. Pitt, S.N. MacMillan, P.J. Milner, High-concentration self-assembly of zirconium-and hafnium-based metal–organic materials, J. Am. Chem. Soc. 145 (24) (2023) 13273–13283.
[20] S. Bazzazan, K. Moeinabadi-Bidgoli, Z.A. Lalami, S. Bazzazan, M. Mehrarya, F.E. Yeganeh, et al., Engineered UIO-66 metal-organic framework for delivery of curcumin against breast cancer cells: an in vitro evaluation, J. Drug Deliv. Sci. Technol. 79 (2023) 104009.
[21] C. He, K. Lu, D. Liu, W. Lin, Nanoscale metal–organic frameworks for the co-delivery of cisplatin and pooled siRNAs to enhance therapeutic efficacy in drug-resistant ovarian cancer cells, J. Am. Chem. Soc. 136 (14) (2014) 5181–5184.
[22] J. Li, F. Lu, X. Shao, B. You, 5-FU@ DHA-UIO-66-NH2 potentiates chemotherapy sensitivity of breast cancer cells through a microRNA let-7a-dependent mechanism, Ann. Transl. Med. 9 (24) (2021).
[23] D.B. Trushina, A.Y. Sapach, O.A. Burachevskaia, P.V. Medvedev, D.N. Khmelenin, T.N. Borodina, et al., Doxorubicin-loaded core–shell UiO-66@ SiO2 metal–organic frameworks for targeted cellular uptake and cancer treatment, Pharmaceutics 14 (7) (2022) 1325.
[24] L. Larasati, W.W. Lestari, M. Firdaus, Dual-action Pt (IV) prodrugs and targeted delivery in metal-organic frameworks: overcoming cisplatin resistance and improving anticancer activity, Bull. Chem. Soc. Jpn. 95 (11) (2022) 1561–1577.
[25] C. Orellana-Tavra, E.F. Baxter, T. Tian, T.D. Bennett, N.K. Slater, A.K. Cheetham, D. Fairen-Jimenez, Amorphous metal–organic frameworks for drug delivery, Chem. Commun. 51 (73) (2015) 13878–13881.

[26] M. Nasrabadi, M.A. Ghasemzadeh, M.R.Z. Monfared, The preparation and characterization of UiO-66 metal–organic frameworks for the delivery of the drug ciprofloxacin and an evaluation of their antibacterial activities, New J. Chem. 43 (40) (2019) 16033–16040.
[27] M. Parsaei, K. Akhbari, Magnetic UiO-66-NH2 core–shell nanohybrid as a promising carrier for quercetin targeted delivery toward human breast cancer cells, ACS Omega 8 (44) (2023) 41321–41338.
[28] O. Susilowati, W.W. Lestari, M. Handayani, C. Sukowati, C. Tiribelli, L.S. Crocè, et al., One pot synthesis of UiO-66-NH2 containing curcumin and cytotoxic evaluation toward liver cancer cells, Mater. Lett. 365 (2024) 136460.
[29] A. Hashemzadeh, F. Amerizadeh, F. Asgharzadeh, G.P. Drummen, S.M. Hassanian, M. Landarani, et al., Magnetic amine-functionalized UiO-66 for oxaliplatin delivery to colon cancer cells: in vitro studies, J. Cluster Sci. 33 (5) (2022) 2345–2361.
[30] N. Rakhshani, N. Hassanzadeh Nemati, A. Ramezani Saadatabadi, S. Sadrnezhaad, Fabrication and evaluation of controlled release of Doxorubicin loaded UiO-66-NH2 metal organic frameworks, Int. J. Eng. 34 (8) (2021) 1874–1881.
[31] N. Rakhshani, N. Hassanzadeh Nemati, A.R. Saadatabadi, S.K. Sadrnezhaad, Fabrication of novel poly(N-vinylcaprolactam)-coated UiO-66-NH2 metal organic framework nanocarrier for the controlled release of doxorubicin against A549 lung cancer cells, J. Drug Deliv. Sci. Technol. 66 (2021) 102881.
[32] R. George Boyle, S. Travers, Hypoxia: targeting the tumour, Anti Cancer Agents Med. Chem. 6 (4) (2006) 281–286.
[33] Y.G. Assaraf, C.P. Leamon, J.A. Reddy, The folate receptor as a rational therapeutic target for personalized cancer treatment, Drug Resist. Updates 17 (4–6) (2014) 89–95.
[34] L.S. Boogerd, M.C. Boonstra, A.-J. Beck, A. Charehbili, C.E. Hoogstins, H.A. Prevoo, et al., Concordance of folate receptor-α expression between biopsy, primary tumor and metastasis in breast cancer and lung cancer patients, Oncotarget 7 (14) (2016) 17442.
[35] A. Farboudi, K. Mahboobnia, F. Chogan, M. Karimi, A. Askari, S. Banihashem, et al., UiO-66 metal organic framework nanoparticles loaded carboxymethyl chitosan/poly ethylene oxide/polyurethane core-shell nanofibers for controlled release of doxorubicin and folic acid, Int. J. Biol. Macromol. 150 (2020) 178–188.
[36] S. Soman, S. Kulkarni, P. Vineeth, S.D. George, S. Mutalik, Harnessing nanotechnology for breast cancer management: UiO-66 (NH2) metal-organic frameworks functionalized with chitosan and folic acid for the efficient delivery of doxorubicin, Nano-Structures & Nano-Objects 40 (2024) 101360.
[37] H. Zeng, C. Xia, B. Zhao, M. Zhu, H. Zhang, D. Zhang, et al., Folic acid–functionalized metal-organic framework nanoparticles as drug carriers improved bufalin antitumor activity against breast cancer, Front. Pharmacol. 12 (2022) 747992.
[38] A. Hashemi, S. Reza hayat-gheibi, F. Baghbani-Arani, Co-delivery of epirubicin and letrozole using a metal-organic framework nanoparticle in breast cancer therapy, J. Drug Deliv. Sci. Technol. (2024) 105515.
[39] S.N. Tambat, P.K. Sane, S. Suresh, N. Varadan, A.B. Pandit, S.M. Sontakke, Hydrothermal synthesis of NH2-UiO-66 and its application for adsorptive removal of dye, Adv. Powder Technol. 29 (11) (2018) 2626–2632.
[40] M. Safari Sharafshadeh, F. Tafvizi, P. Khodarahmi, S. Ehtesham, Folic acid-functionalized PEGylated niosomes co-encapsulated cisplatin and doxoribicin exhibit enhanced anticancer efficacy, Cancer Nanotechnology 15 (1) (2024) 1–25.
[41] Z. Asghari Lalami, F. Tafvizi, V. Naseh, M. Salehipour, Fabrication, optimization, and characterization of pH-responsive PEGylated nanoniosomes containing gingerol for enhanced treatment of breast cancer, N. Schmied. Arch. Pharmacol. 396 (12) (2023) 3867–3886.
[42] N. Mahdizadeh, M. Khorshid Shabestari, F. Tafvizi, P. Khodarahmi, Delivery of letrozole-encapsulated niosomes via a 3D bioprinting gelatin–alginate scaffold for potential breast cancer treatment, Cancer Nanotechnology 15 (1) (2024) 33.
[43] A. Mohammadi Shivyari, F. Tafvizi, H. Noorbazargan, Anti-cancer effects of biosynthesized zinc oxide nanoparticles using Artemisia scoparia in Huh-7 liver cancer cells, Inorganic and Nano-Metal Chemistry 52 (3) (2022) 375–386.
[44] M. Dolati, F. Tafvizi, M. Salehipour, T.K. Movahed, P. Jafari, Inhibitory effects of probiotic Bacillus coagulans against MCF7 breast cancer cells, Iran. J. Microbiol. 13 (6) (2021) 839.
[45] S. Rostami, F. Tafvizi, H.R.K. Manjili, High efficacy of tamoxifen-loaded L-lysine coated magnetic iron oxide nanoparticles in cell cycle arrest and anti-cancer activity for breast cancer therapy, Bioimpacts: BI 12 (4) (2021) 301.
[46] M. Fatemizadeh, F. Tafvizi, F. Shamsi, S. Amiri, A. Farajzadeh, I. Akbarzadeh, Apoptosis induction, cell cycle arrest and anti-cancer potential of tamoxifen-curcumin loaded niosomes against MCF-7 cancer cells, Iran J Pathol 17 (2) (2022) 183–190.
[47] M. Ronaghi, R. Hajibeygi, R. Ghodsi, A. Eidi, R. Bakhtiari, Preparation of UiO-66 loaded Letrozole nano-drug delivery system: enhanced anticancer and apoptosis activity, AMB Express 14 (1) (2024) 38.
[48] D. Giliopoulos, A. Zamboulis, D. Giannakoudakis, D. Bikiaris, K. Triantafyllidis, Polymer/metal organic framework (MOF) nanocomposites for biomedical applications, Molecules 25 (1) (2020) 185.
[49] Z. Khatibi, N.M. Kazemi, S. Khaleghi, Targeted and biocompatible NMOF as efficient nanocomposite for delivery of methotrexate to colon cancer cells, J. Drug Deliv. Sci. Technol. 73 (2022) 103441.
[50] M. Longmire, P.L. Choyke, H. Kobayashi, Clearance Properties of Nano-Sized Particles and Molecules as Imaging Agents: Considerations and Caveats, 2008.
[51] Z. Sabouri, M. Sabouri, M.S. Amiri, M. Khatami, M. Darroudi, Plant-based synthesis of cerium oxide nanoparticles using Rheum turkestanicum extract and evaluation of their cytotoxicity and photocatalytic properties, Mater. Technol. 37 (8) (2022) 555–568.
[52] P. Khandel, S.K. Shahi, D.K. Soni, R.K. Yadaw, L. Kanwar, Alpinia calcarata: potential source for the fabrication of bioactive silver nanoparticles, Nano convergence 5 (2018) 1–17.
[53] A. Khatri, P.S. Rana, Visible light photocatalysis of methylene blue using cobalt substituted cubic NiO nanoparticles, Bull. Mater. Sci. 42 (4) (2019) 141.
[54] G.E. Cinay, P. Erkoc, M. Alipour, Y. Hashimoto, Y. Sasaki, K. Akiyoshi, S. Kizilel, Nanogel-integrated pH-responsive composite hydrogels for controlled drug delivery, ACS Biomater. Sci. Eng. 3 (3) (2017) 370–380.
[55] A.R. Chowdhuri, D. Laha, S. Chandra, P. Karmakar, S.K. Sahu, Synthesis of multifunctional upconversion NMOFs for targeted antitumor drug delivery and imaging in triple negative breast cancer cells, Chem. Eng. J. 319 (2017) 200–211.
[56] Z. Hasan, M. Tong, B.K. Jung, I. Ahmed, C. Zhong, S.H. Jhung, Adsorption of pyridine over amino-functionalized metal–organic frameworks: attraction via hydrogen bonding versus base–base repulsion, J. Phys. Chem. C 118 (36) (2014) 21049–21056.
[57] X. Ji, X. Song, J. Li, Y. Bai, W. Yang, X. Peng, Size control of gold nanocrystals in citrate reduction: the third role of citrate, J. Am. Chem. Soc. 129 (45) (2007) 13939–13948.
[58] A. Nel, T. Xia, L. Madler, N. Li, Toxic potential of materials at the nanolevel, Sci. Technol. Humanit. 311 (5761) (2006) 622–627.
[59] M.E. Selim, A.A. Hendi, Gold nanoparticles induce apoptosis in MCF-7 human breast cancer cells, Asian Pac. J. Cancer Prev. APJCP 13 (4) (2012) 1617–1620.
[60] I.A. Lazaro, R.S. Forgan, Application of zirconium MOFs in drug delivery and biomedicine, Coord. Chem. Rev. 380 (2019) 230–259.
[61] M. Gholami, M. Darroudi, A. Hekmat, M. Khazaei, Five-FU@ CuS/NH2-UiO-66 as a drug delivery system for 5-fluorouracil to colorectal cancer cells, J. Biochem. Mol. Toxicol. 36 (9) (2022) e23145.
[62] M. Gholami, A. Hekmat, M. Khazaei, M. Darroudi, OXA-CuS@ UiO-66-NH2 as a drug delivery system for Oxaliplatin to colorectal cancer cells, J. Mater. Sci. Mater. Med. 33 (3) (2022) 26.
[63] Z. Wan, C. Li, J. Gu, J. Qian, J. Zhu, J. Wang, et al., Accurately controlled delivery of temozolomide by biocompatible uio-66-nh2 through ultrasound to enhance the antitumor efficacy and attenuate the toxicity for treatment of malignant glioma, Int. J. Nanomed. (2021) 6905–6922.
[64] I. Abánades Lázaro, S. Haddad, J.M. Rodrigo-Muñoz, C. Orellana-Tavra, V. Del Pozo, D. Fairen-Jimenez, R.S. Forgan, Mechanistic investigation into the selective anticancer cytotoxicity and immune system response of surface-functionalized, dichloroacetate-loaded, UiO-66 nanoparticles, ACS Appl. Mater. Interfaces 10 (6) (2018) 5255–5268.
[65] M.S. de Almeida, E. Susnik, B. Drasler, P. Taladriz-Blanco, A. Petri-Fink, B. Rothen-Rutishauser, Understanding nanoparticle endocytosis to improve targeting strategies in nanomedicine, Chem. Soc. Rev. 50 (9) (2021) 5397–5434.
[66] A. Hashemzadeh, F. Amerizadeh, F. Asgharzadeh, M. Darroudi, A. Avan, S.M. Hassanian, et al., Delivery of oxaliplatin to colorectal cancer cells by folate-targeted UiO-66-NH2, Toxicol. Appl. Pharmacol. 423 (2021) 115573.

[67] N. Kunac, N. Filipović, S. Kostić, K. Vukojević, The expression pattern of Bcl-2 and Bax in the tumor and stromal cells in colorectal carcinoma, Medicina 58 (8) (2022) 1135.
[68] H. Sultana, J. Kigawa, Y. Kanamori, H. Itamochi, T. Oishi, S. Sato, et al., Chemosensitivity and p53–Bax pathway-mediated apoptosis in patients with uterine cervical cancer, Ann. Oncol. 14 (2) (2003) 214–219.
[69] W. Li, Y. Wang, Y. Song, L. Xu, J. Zhao, B. Fang, A preliminary study of the effect of curcumin on the expression of p53 protein in a human multiple myeloma cell line, Oncol. Lett. 9 (4) (2015) 1719–1724.
[70] M. Moawad, G.M. Nasr, A.S. Osman, E.S. Shaker, Curcumin nanocapsules effect in apoptotic processes, gene expression, and cell cycle on Hep-G2 cell lines, Int. J. Immunopathol. Pharmacol. 37 (2023) 03946320231176396.
[71] Q. Hu, T. Huang, Regulation of the cell cycle by ncRNAs affects the efficiency of CDK4/6 inhibition, Int. J. Mol. Sci. 24 (10) (2023) 8939.
[72] Y. Sun, Y. Liu, X. Ma, H. Hu, The influence of cell cycle regulation on chemotherapy, Int. J. Mol. Sci. 22 (13) (2021) 6923.
[73] I. Kazazi, F. Ashrafi, M. Malekloo, Synthesis of Gingerol-loaded Uio-66 nanoparticles and its anti-cancer effect against gastric cancer cell line (AGS), Mol. Biol. Rep. 50 (4) (2023) 3503–3513.
[74] Y. Pan, W. Shan, H. Fang, M. Guo, Z. Nie, Y. Huang, S. Yao, Sensitive and visible detection of apoptotic cells on Annexin-V modified substrate using aminophenylboronic acid modified gold nanoparticles (APBA-GNPs) labeling, Biosens. Bioelectron. 52 (2014) 62–68.
[75] N. Martinho, T.C.B. Santos, H.F. Florindo, L.C. Silva, Cisplatin-membrane interactions and their influence on platinum complexes activity and toxicity, Front. Physiol. 9 (2018) 1898.
[76] D. Payet, F. Gaucheron, M. Sip, M. Leng, Instability of the monofunctional adducts in cis-[Pt (NH 3) 2 (N7-N-methyl-2-diazapyrenium) Cl] 2+;-modified DNA: rates of cross-linking reactions in cis-platinummodified DNA, Nucleic Acids Res. 21 (25) (1993) 5846–5851.
[77] S.M. Cohen, S.J. Lippard, Cisplatin: from DNA Damage to Cancer Chemotherapy, 2001.
[78] T. Imamura, H. Izumi, G. Nagatani, T. Ise, M. Nomoto, Y. Iwamoto, K. Kohno, Interaction with p53 enhances binding of cisplatin-modified DNA by high mobility group 1 protein, J. Biol. Chem. 276 (10) (2001) 7534–7540.
[79] D.B. Zamble, Y. Mikata, C.H. Eng, K.E. Sandman, S.J. Lippard, Testis-specific HMG-domain protein alters the responses of cells to cisplatin, J. Inorg. Biochem. 91 (3) (2002) 451–462.
[80] M. Petrović, D. Todorović, Biochemical and molecular mechanisms of action of cisplatin in cancer cells, Facta Univ. – Ser. Med. Biol. (2016) 12–18.
[81] J. Gumulec, J. Balvan, M. Sztalmachova, M. Raudenska, V. Dvorakova, L. Knopfova, et al., Cisplatin-resistant prostate cancer model: differences in antioxidant system, apoptosis and cell cycle, Int. J. Oncol. 44 (3) (2013) 923–933.
[82] S.Y. Saad, T.A. Najjar, M. Alashari, Role of non-selective adenosine receptor blockade and phosphodiesterase inhibition in cisplatin-induced nephrogonadal toxicity in rats, Clin. Exp. Pharmacol. Physiol. 31 (12) (2004) 862–867.
[83] G. Nuñez, M.A. Benedict, Y. Hu, N. Inohara, Caspases: the proteases of the apoptotic pathway, Oncogene 17 (25) (1998) 3237–3245.
[84] G.S. Salvesen, J.M. Abrams, Caspase activation–stepping on the gas or releasing the brakes? Lessons from humans and flies, Oncogene 23 (16) (2004) 2774–2784.
[85] S. Elmore, Apoptosis: a review of programmed cell death, Toxicol. Pathol. 35 (4) (2007) 495–516.
[86] K. Kohno, K.-Y. Wang, M. Takahashi, T. Kurita, Y. Yoshida, M. Hirakawa, et al., Mitochondrial transcription factor A and mitochondrial genome as molecular targets for cisplatin-based cancer chemotherapy, Int. J. Mol. Sci. 16 (8) (2015) 19836–19850.
[87] C. Chen, J. Ke, X.E. Zhou, W. Yi, J.S. Brunzelle, J. Li, et al., Structural basis for molecular recognition of folic acid by folate receptors, Nature 500 (7463) (2013) 486–489.
[88] P. Fotouhi, S. Sohrabi, N. Nosrati, A.Z. Vaziri, S. Khaleghi, A. Narmani, et al., Surface modified and rituximab functionalized PAMAM G4 nanoparticle for targeted imatinib delivery to leukemia cells: in vitro studies, Process Biochem. 111 (2021) 221–229.
[89] E. Ahmadian, S.M. Dizaj, S. Sharifi, S. Shahi, R. Khalilov, A. Eftekhari, M. Hasanzadeh, The potential of nanomaterials in theranostics of oral squamous cell carcinoma: recent progress, TrAC, Trends Anal. Chem. 116 (2019) 167–176.
[90] M. Kielbik, D. Krzyzanowski, B. Pawlik, M. Klink, Cisplatin-induced ERK1/2 activity promotes G1 to S phase progression which leads to chemoresistance of ovarian cancer cells, Oncotarget 9 (28) (2018) 19847–19860.
[91] V. Velma, S.R. Dasari, P.B. Tchounwou, Low doses of cisplatin induce gene alterations, cell cycle arrest, and apoptosis in human promyelocytic leukemia cells, Biomark. Insights 11 (2016) 113–121.
[92] S. Sai, G. Vares, E.H. Kim, K. Karasawa, B. Wang, M. Nenoi, et al., Carbon ion beam combined with cisplatin effectively disrupts triple negative breast cancer stem-like cells in vitro, Mol. Cancer 14 (2015) 1–13.
[93] X. Zhong, X. Li, G. Wang, Y. Zhu, G. Hu, J. Zhao, et al., Mechanisms underlying the synergistic effect of SU5416 and cisplatin on cytotoxicity in human ovarian tumor cells, Int. J. Oncol. 25 (2) (2004) 445–451.
[94] S. Lomonaco, The Role of Nucleotide Excision Repair in DNA Damage Mediated Apoptosis and Cell Cycle Regulation, Wayne State University, 2007.
[95] T. Zhang, Y. Sun, J. Cao, J. Luo, J. Wang, Z. Jiang, P. Huang, Intrinsic nucleus-targeted ultra-small metal-organic framework for the type I sonodynamic treatment of orthotopic pancreatic carcinoma, J. Nanobiotechnol. 19 (1) (2021) 315.
[96] J.H. Joo, A.M. Jetten, Molecular mechanisms involved in farnesol-induced apoptosis, Cancer Lett. 287 (2) (2010) 123–135.
[97] J. Cheng, H. Cao, Y. Xu, Y. Yang, Y. He, H. Wang, In situ monitoring of dynamic photocatalysis of metal–organic frameworks by three-dimensional shell-isolated nanoparticle-enhanced Raman spectroscopy, Anal. Chem. 94 (14) (2022) 5699–5706.
[98] P. Zhang, A. Fischer, Y. Ouyang, J. Wang, Y.S. Sohn, R. Nechushtai, et al., Aptamer-modified DNA tetrahedra-gated metal–organic framework nanoparticle carriers for enhanced chemotherapy or photodynamic therapy, Chem. Sci. 12 (43) (2021) 14473–14483.
[99] M. Sk, S. Banesh, V. Trivedi, S. Biswas, Selective and sensitive sensing of hydrogen peroxide by a boronic acid functionalized metal–organic framework and its application in live-cell imaging, Inorg. Chem. 57 (23) (2018) 14574–14581.
[100] N. Tomar, S. Sadri, Jr AW. Cowley, C. Yang, N. Quryshi, V.R. Pannala, et al., A thermodynamically-constrained mathematical model for the kinetics and regulation of NADPH oxidase 2 complex-mediated electron transfer and superoxide production, Free Radic. Biol. Med. 134 (2019) 581–597.
[101] S. Sadri, N. Tomar, C. Yang, S.H. Audi, A.W. Cowley, R.K. Dash, Mechanistic computational modeling of the kinetics and regulation of NADPH oxidase 2 assembly and activation facilitating superoxide production, Free Radic. Res. 54 (10) (2020) 695–721.
[102] W. Zeng, Q. Li, T. Wan, C. Liu, W. Pan, Z. Wu, et al., Hyaluronic acid-coated niosomes facilitate tacrolimus ocular delivery: mucoadhesion, precorneal retention, aqueous humor pharmacokinetics, and transcorneal permeability, Colloids Surf. B Biointerfaces 141 (2016) 28–35.